Photometry of Outer-belt Objects

by

Gautham S. Narayan

Submitted to the Department of Physics
in partial fulfillment of the requirements for Research Honors

at

Illinois Wesleyan University

April 2005

Author: _____

<div align="right">Department of Physics</div>

Certified by: _____

<div align="right">Dr. Linda M. French
Reader</div>

Certified by: _____

<div align="right">Dr. Narendra K. Jaggi
Reader</div>

Certified by: _____

<div align="right">Dr. Ram S. Mohan
Reader</div>

Certified by: _____

<div align="right">Dr. Gabriel C. Spalding
Reader</div>

CONTENTS

ABSTRACT

We present results from multi-wavelength observations of outer-belt asteroid 279 Thule and comet C/2002 CE$_{10}$ (LINEAR). The orbital elements of the second object, formerly classified as asteroid 2002 CE$_{10}$, at first led to its identification with a group of asteroids called the Damocloids. The Damocloids' orbits are similar to Halley family comets (HFCs), and there is suspicion that the Damocloids are inactive HFC nuclei. Following observations by the 8.2 m Japanese Subaru telescope in August 2003, which determined that 2002 CE$_{10}$ had a characteristic tail (Takato et al; 2003), it was re-classified as comet C/2002 CE$_{10}$ (LINEAR).

We observed these and other objects with filters close to the Johnson-Kron-Cousins BVRI filters corresponding to the blue, visible, red, and near-IR wavelengths using the 0.9m SMARTS telescope at Cerro-Tololo Inter-American Observatory during October 2003. Using the image reduction routines (*imred*) of the Image Reduction and Analysis Facility (NOAO X11/IRAF), we removed the bias caused by dark currents, and flat fielded the data to improve the signal-to-noise ratio (SNR).

Instrumental magnitudes for all objects were extracted using the aperture photometry package (*apphot*). Landolt standard stars were used to solve the transformation equations and extract extinction coefficients. Photometric calibration routines (*photcal*) allowed us to use the extinction coefficients and instrumental magnitudes to determine magnitudes in the Landolt standard system. We computed absolute magnitudes for 279 Thule and C/2002 CE$_{10}$ (LINEAR) in the VR bands by correcting for the changing geocentric distance, heliocentric distance, and solar phase of the object. 279 Thule was found to have a mean absolute visual magnitude of 8.66±0.01 and a V-R color of 0.44±0.03, when corrected for solar phase using the standard IAU phase relation (Bowell et al; 1989). We discuss the suitability of the standard phase relation for 279 Thule. We place constraints on the size of the objects. We determine the rotation period for 279 Thule to be 7.6±0.5 hrs, using an implementation of the phase dispersion minimization (PDM) algorithm first developed by Stellingwerf (1978). It is likely that observations of C/2002 CE$_{10}$ (LINEAR) have been contaminated by near nucleus coma.

1. INTRODUCTION

Outer-belt asteroids are small objects left over from the material that accreted into the planets. Since they presently have a low frequency of collisions, the surface compositions of several primitive asteroids may be representative of the composition of the early solar nebula. Some asteroids are more thermally evolved because of their proximity to the sun, and may be able to shed light on early solar system processes.

Comet nuclei are especially interesting since they are likely carriers of material captured in the sun's proto-planetary disk some 4.5 billion years ago. However, their small sizes make them very difficult to study, as their nuclei do not scatter many photons. As they approach the sun, comets develop a coma around their nucleus, which can swamp the signal from it, making its properties very hard to determine. When they are further away from the sun, they are not bright enough for photometric purposes. Thus, very few cometary nuclei have been studied using ground-based observations. Ground-based studies concentrate on cometary nuclei with low out-gassing even near perihelion, such as P/Encke (Fernandez et al; 2000).

Here we present results from Johnson-Kron-Cousins BVRI observations of two outer-belt objects, Asteroid 279 Thule and Comet C/2002 CE_{10} (LINEAR). A table of orbital elements for the two objects is given below.

TABLE 1.1: ORBITAL ELEMENTS OF OBSERVED OBJECTS

(Source: Minor Planet Center, IAU)

Name	a (AU)	e	i (deg)	q (AU)	P (years)
279 Thule	4.277	0.012	2.338	4.224	8.84
C/2002 CE_{10} (LINEAR)	9.81	0.7914	145.45	2.04	30.8

a = semi-major axis e = eccentricity i = inclination q = perihelion distance P = orbital period

Zappala et al. (1989) have determined a rotation period of 7.44 hrs for 279 Thule. Spectroscopic observations have determined that it is a D-type asteroid (Fitzsimmons et al; 1990). Further, the same study found that 279 Thule exhibited interesting features in the absorption spectra at 416, 441 and 515 nm that do not correspond to any known asteroidal absorption features or known atmospheric absorption bands (Lagerkvist et al; 1990). D-type asteroids appear to be redder than most outer-belt asteroids and are thought to be more primitive than any known meteorite; their unusual redness is thought to be evidence that their surfaces are composed of "supercarbonaceous" chondrites (Vilas et al; 1985) and have not been subject to considerable heating. 279 Thule is also the only asteroid in a 4:3 orbital resonance with Jupiter.

C/2002 CE$_{10}$ LINEAR was discovered in February 2002 (McNaught et al; 2002). Classified as an asteroid until observations in August 2003 by the 8.2 m Japanese Subaru telescope that determined that it had a characteristic tail (Takato et al; 2003), C/2002 CE$_{10}$ (LINEAR) is especially interesting as its orbital elements are similar to those of Halley family comets (HFCs) and the Damocloid family of asteroids. The similarity between HFC and the Damocloid distribution of eccentricity and inclination suggest that the Damocloids are inactive Halley family comet nuclei (Asher et al; 1994). In addition, the distribution of inclinations of HFCs and the Damocloids (see Fig. 1.1) is clearly distinct from that of Jupiter family comets (JFCs) (Jewitt, 2005) and numerical simulations indicate that Damocloids are unlikely to be former JFCs whose orbits have evolved into orbits that resemble HFCs (Levinson and Duncan, 1997). The theory that Damocloids are dead HFC nuclei is supported by the observations of C/2002 CE$_{10}$ (LINEAR) and observations of C/2001 OG$_{108}$ (LONEOS) (Abell et al; 2005), C/2002 VQ$_{94}$ (LINEAR) (Jewitt, 2005) and 2060 Chiron (Meech et al; 1989). These objects were initially classified as Damocloids and were later observed exhibiting cometary activity.
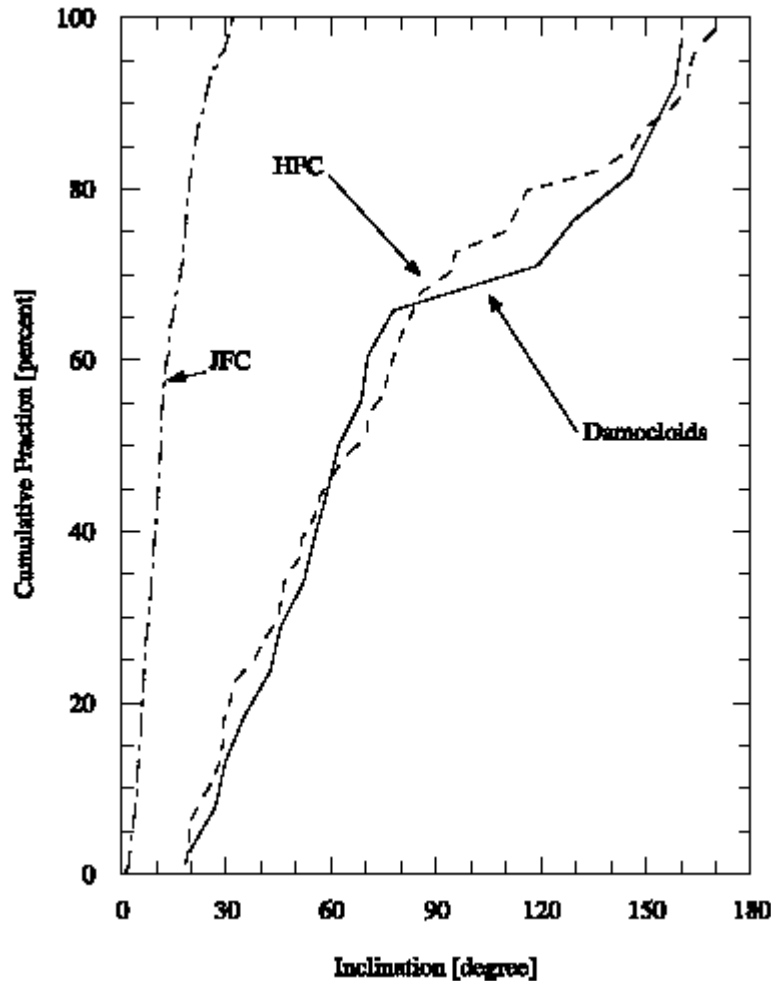
Figure 1.1: Cumulative distributions of inclinations of various outer-belt families. The Damocloid sample (solid line) consists of 20 objects with $T_J \leq 2$ and is very similar to the HFC sample (dashed line) that consists of 42 comets with $T_J \leq 2$, and periods over 200 years. The JFC sample (dashed-dotted line) consists of 240 comets with $2 \leq T_J \leq 3$, and does not appear to be related to the HFCs or Damocloids. (Source: Jewitt, 2005)

The Tisserand parameter, introduced in the late 19th century by the French mathematician Felix Tisserand in his classic work "Traité de mécanique céleste", can be used to distinguish between different outer-belt groups. 'T_J' relative to Jupiter, is defined as

$$T_J = \frac{a_J}{a} + 2 \left(cos\ i \right) \sqrt{\left(1 - e^2 \right) \frac{a}{a_J}}$$

(1.1)

where 'a' is the semi-major axis and, 'e' is the eccentricity and 'i' is the inclination of the orbit. The semi-major axis of Jupiter 'a_J' is 5.2 AU. This definition assumes that Jupiter is in a circular orbit, and ignores the gravitational effects of other planets, which have long-term effects. However, as the Tisserand parameter depends only on semi-major axis, eccentricity and inclination it can be treated as a constant for an outer-belt object. HFCs and Damocloids both have $T_J \leq 2$, while JFCs exhibit $2 \leq T_J \leq 3$. Most asteroids have $T_J > 3$; the Tisserand parameter clearly reflects the distinctions between the different groups.

Broadband photometry is a versatile tool that can be used to determine asteroid rotation periods, constrain shape, and determine surface colors, thus contributing to an understanding of asteroid surface chemical composition. It is possible to use photometry even when luminosities are insufficient to do spectroscopy or spectrophotometry, and therefore with relatively small aperture telescopes. Outer-belt objects are generally not spherically symmetric, and they have angular momentum about an internal axis; therefore, the area they present to the earth and the amount of sunlight they reflect varies periodically with time. By determining its absolute magnitude[1.1] at different times, we can find the rotation period of the asteroid, provided we have sufficient phase coverage. Using the magnitude variation of the lightcurve, we can place limits on the ratio of the diameters of the area the object presents towards us. In addition, if radar observations are present or assumptions about the fraction of the light reflected (or albedo) are made, we can place limits on the lengths of these diameters.

[1.1] The magnitude equation and other photometric terms are discussed in Appendix A. The author uses the terms instrumental magnitude, apparent magnitude and absolute magnitude wherever more than one type of magnitude arises to avoid confusion.

2. INSTRUMENTATION AND OBSERVATIONS

2.1 The Optical Path and Measurement Chain

We made all observations using the 0.9-m Cassegrain SMARTS telescope on an off-axis asymmetric mount at the Cerro Tololo Inter-American Observatory (CTIO), La Serena, Chile, from October 14-20th, 2003. A thinned, back-illuminated, 2048x2046 Tektronix QUAD CCD with anti-reflective coatings to improve performance in the near-IR is located at the f/13.5 Cassegrain focus. The CCD has an image scale of 0.396″ pixel[-1]; the total field size is therefore 13.5′. The CCD has better than 70% quantum efficiency at $\lambda \sim 0.7\mu m$[2.1](Walker, 2000).

The CCD is automatically shuttered when not observing, or "integrating." The shutter unit has a 10 cm clear aperture. Shutter speed is high and the difference between exposure times at the center of field and the corners is reported to be ~50 ms. We neglect this difference as our integration times are greater by at least three orders of magnitude.

The detector, comprising the CCD and the readout electronics, was cooled with liquid nitrogen in order to reduce background Johnson noise that manifests as dark currents in the detector. Two independent filter wheels, mounted in front of the fused silica window of the CCD, hold one 3x3 inch "color balanced" (CB) filter and four 3x3 inch Johnson-Kron-Cousins BVRI filters respectively. We use the CB filter exclusively for "dome-flats"; we rotate the filter out of the optical path for all other observations. Dome-flats are discussed later in the chapter. All of the filters are less than 0.6 cm thick.

QUAD mode allows the CCD to be readout in parallel through four amplifiers, thus decreasing readout times substantially. This decrease in readout times comes with a price since the procedure used for image processing becomes more complex to account for multiple amplifiers with different properties. The amplifier continues to readout the CCD along a row even after all the active pixels are binned. This "overscan region" is used to estimate the "bias level" of a row during the readout. The bias level is discussed later on in this chapter. The use of four amplifiers results in four separate overscan regions that are combined at the center of the image.

A 16-bit analog-digital converter then digitizes the data readout by the amplifiers. At this point, the data is measured in "analog-to-digital units" (ADU) and can take values between 0 and 2^{16}-1 i.e. 0 to 65535. The ratio of the number of ADUs per electron read is the signal gain; however, it is conventional to refer to the inverse gain in e[-]/ADU as the gain. The data is then transmitted via a serial fiber-optic cable to a spool file where it is converted to an image file in .pix format (see Fig. 2.1). An associated "image header" text file in .imh format is simultaneously created.[2.2]

[2.1] Basic information on CCDs is included in Appendix B. The Tek2K QE curve and transmission curves for each of the filters is also included.
[2.2] We moved data from CTIO to Illinois Wesleyan University using the Flexible Image Transport System (.fits) format, which combines image file and image header into a single file. These are automatically extracted during image processing.
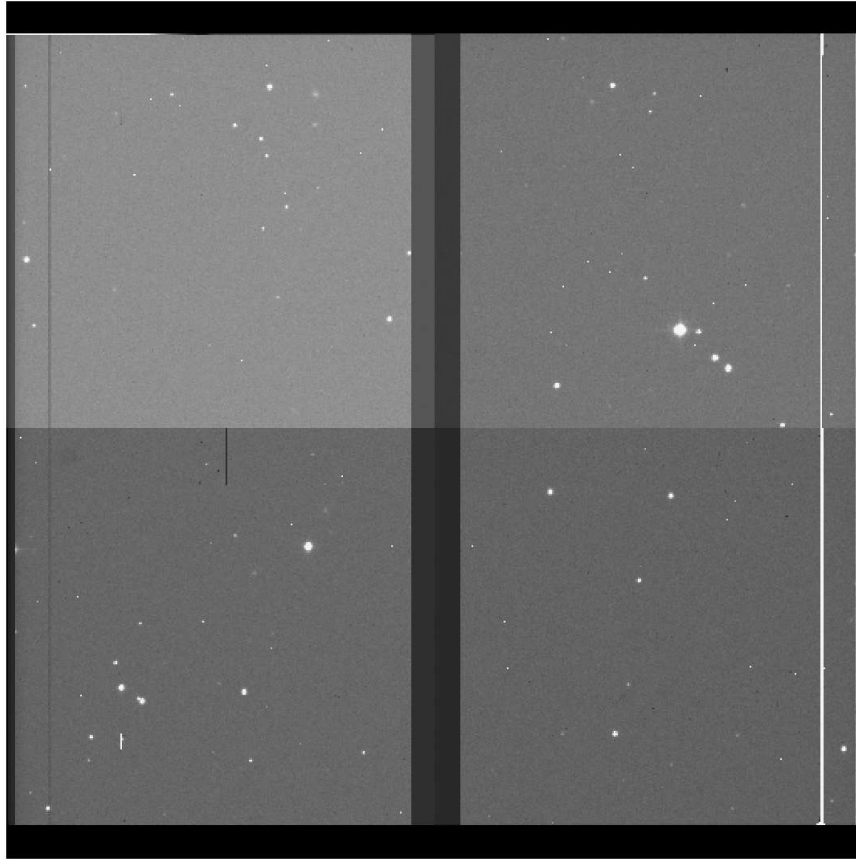
Figure 2.1: A typical raw output image file. Four separate amplifiers readout separate regions of the CCD. The different contrasts in each region are the result of different electrical backgrounds or bias in each region. The overscan region generated by each amplifier is combined together to form a dark band at the center of the image. Rows that have not been illuminated cause the dark regions at the top and bottom of the frame, which must be trimmed. Some columns inside the frame are damaged and are displayed entirely white or black. This image is a 240-second observation in the 'V' filter.

The Array Controller (ARCON) system manages the CCD and the readout electronics and provides the interface between the observer and detector, via software run from a Sun Microsystems UltraSparc 5, using the Solaris 8 OS with the Open Windows desktop environment. ARCON writes CCD information as well as observation specific data such as integration time, filters used, telescope pointing position and weather information into the image header.

ARCON monitors all shutter open and close time measurements and synchronizes with the CTIO clock every hour. The CTIO clock is synchronized six times a day with the two U.S Naval Observatory servers as well as five independent timeservers and corrections are applied for packet-transmission time. ARCON reports times to a hundredth of a second and writes this information to header of each of the data frames or images. Fig. 2.2 shows a schematic of the optical path and measurement chain.
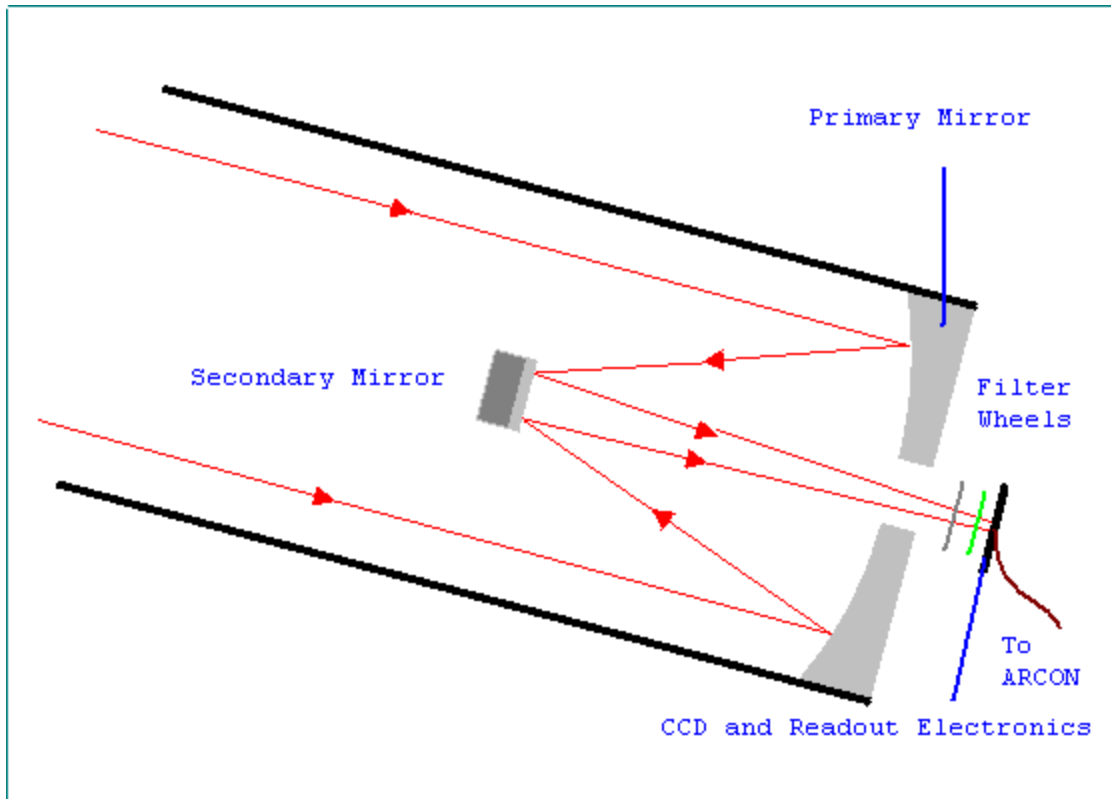
Figure 2.2: A schematic of the optical path and the measurement chain. Light from the target object is reflected by the primary mirror onto the secondary and passes through the two filter wheels, before coming to focus on the CCD. ARCON controls all detector operations, from when the shutter opens, the length of an observation, readout of the CCD and saving the data to disk. It also interfaces with the TCS and focus controller (not shown).

2.2 Auxiliary Hardware

The telescope has a permanently installed, Peltier cooled CCD-based autoguider that images an off-axis field approximately 12'x3' in size. The guider can only scan in 1-D and the usable field is about 4'x3' in size. The guider can be used to acquire and lock on to a star in the field and helps correct errors in the telescope's pointing when the telescope is tracked siderealy. Software calculates corrections and applies them to computer-controlled motors that are independent of the primary tracking motors. Pointing and focus are independent of the detector and autoguider controls. Telescope pointing is computer-controlled via the Telescope Control System (TCS) and the observer can manually override the TCS system. The focus is entirely manually controlled. ARCON is however, configured to read telescope focus and pointing information, which is written to the image header.

Much of the above technical information was compiled from various manuals provided to observers by CTIO (Walker, 2000).

2.3 Observed Objects and Observing Procedure

We selected asteroids for our observing schedule from the database maintained at Lowell Observatory, using the Select List of Orbital Parameters (SLOP) routine based on their geocentric distances, Tisserand parameter, estimated apparent magnitude and the distance they rose above the horizon. We generated ephemeredes, based on known orbital elements, using the EF8 routine for these objects. At the time, C/2002 CE$_{10}$ (LINEAR) was still included in the Lowell asteroid database and we were able to use the same routines to search for it and generate its ephemeris. We shall only report on observations of C/2002 CE$_{10}$ (LINEAR) and 279 Thule in VR bands in this work (see Table 2.1).

TABLE 2.2: OBSERVATIONS USED IN PHOTOMETRY

(Source: Minor Planet Center, IAU and Planetary Data System)

Object	UT Date	T_J	r (AU)	Δ (AU)	α (deg)	OBS
	2003 Oct 17		2.387	1.915-1.917	23.7	4
C/2002 CE$_{10}$	2003 Oct 18	-0.853	2.393	1.942-1.943	23.8	4
	2003 Oct 19		2.398	1.966-1.969	23.9	10
	2003 Oct 16		4.317	3.325	1.5	12
	2003 Oct17		4.317	3.327	1.7-1.8	11
279 Thule	2003 Oct 18	3.03	4.317	3.329	2.0	12
	2003 Oct 19		4.317	3.331	2.2-2.3	8
	2003 Oct 20		4.317	3.334	2.5	10

T_J = Tisserand parameter r = heliocentric distance Δ = geocentric distance α = solar phase angle
OBS = number of observations in both V and R

We selected standard stars[2.3] with a wide range of magnitudes from the Landolt catalog (Landolt, 1992). The vast majority of selected standards have been observed 30 times or more on separate nights and rose well above the horizon. We ensured that the selected standards rose at different times during the night, so we could calibrate photometric observations over the entire night. We observed standards when they were close in airmass[2.4] to target fields.

2.4 Bias and Readout Noise in Observations

A typical day on this observing run would begin in the afternoon. Several different types of images had to be taken in order to process the data images. First, we determined the electrical background in the detector by reading out the CCD without opening the shutter or performing any integration. The output image of such a zero second integration is referred to as a "bias frame" or a "zero frame" and gives us the electrical offset or bias level in the detector. The offset is often several hundred ADUs (see Fig. 2.3). Further, it is not constant but is often empirically found to be a function of position on the chip, telescope position, temperature and several other factors (Massey, 1997). Since taking a bias frame involves readout of the detector, any electrical noise generated by the

---

[2.3] A full table of observed standards used for photometry is included in Chapter 4.
[2.4] Further information on the airmass, magnitudes, point spread functions and other photometric terms is provided in Appendix A.

amplifiers and the other readout electronics is also included in the bias level. Readout noise is considered independent of the integration time and signal recorded in the CCD. Therefore, it is a common offset for all the images. We took fifteen bias frames every afternoon.
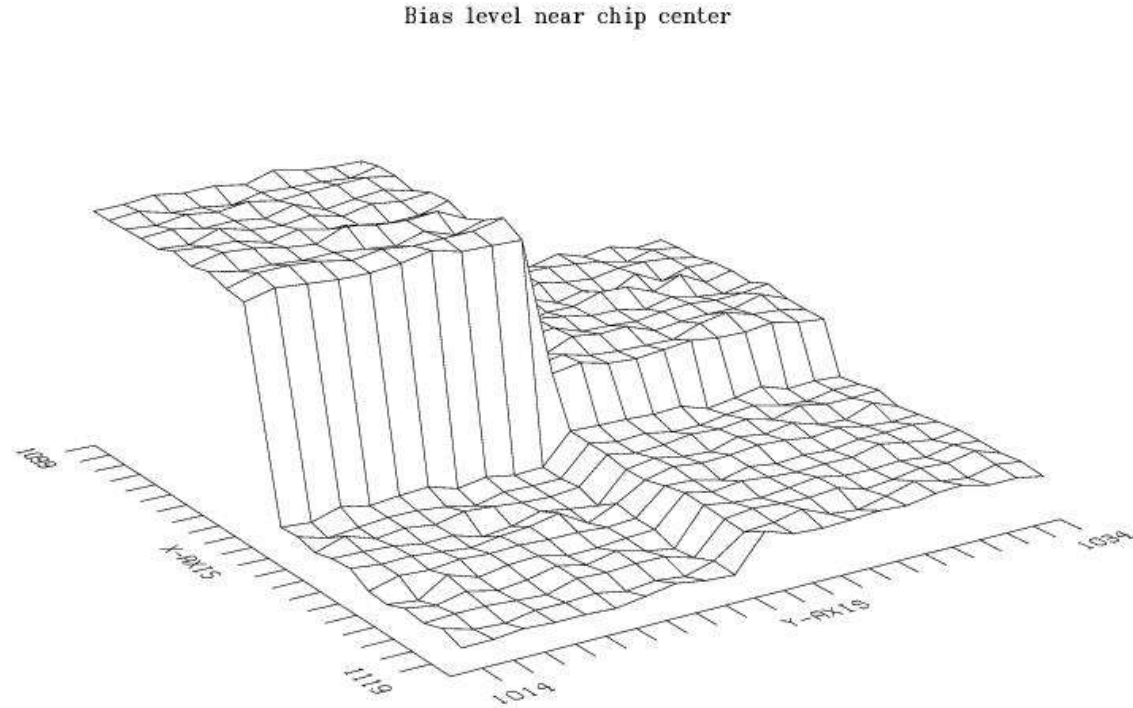
Bias level near chip center

Figure 2.3: A surface plot of the bias level as a function of column and row address taken near the center of a typical unprocessed bias frame. The four separate regions of the image intersect at the center and clearly have different electrical backgrounds. The levels are approximately (from high to low) 635, 553, 521 and 505 ADU.

As the detector is cooled with liquid nitrogen, we neglect any noise generated by thermal currents. As part of standard operating procedure, a "dark frame" was taken without opening the shutter, with an integration time of at least thirty seconds by the telescope operator (telop), before the night's observations, to verify that the detector had been cooled correctly. These were found to be virtually identical to a zero second integration bias frame and demonstrate that dark currents are not a significant contribution to the noise.

2.5 Non-uniform Detector Response and Flat-fields

In general, when a CCD is uniformly illuminated, its response is not uniform and a different signal may be recorded by each pixel. Small-scale variations are usually caused by differences in pixel size. Variations in the thickness of the silicon wafer across the chip, cause large-scale variations in response; this is especially true of thinned CCDs (Massey, 1997). Non-uniformities can also result from dust settled on the primary mirror of the telescope. Even small dust particles on the primary are very far from focus and appear as "donuts" in images (see Fig. 2.4).
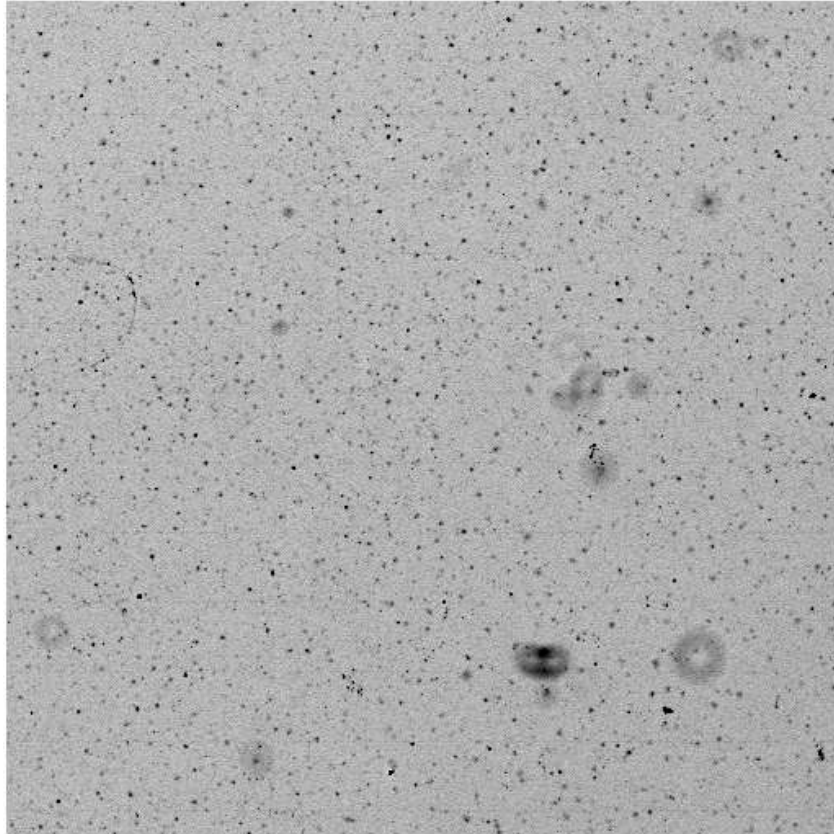
Figure 2.4: A section from a typical flat. Non-uniformities caused by dust in the optical path manifests as "donuts." Variations from pixel to pixel are evident as several pixels readout with different levels, which are displayed as different shades of grey or black. Variations across the entire section exist but are not large enough to cause a large difference in contrast. This image was overscan subtracted, trimmed and bias corrected, as described in Chapter 3.

In order to remove such non-uniformities, we take several "flats" or images with the CCD subject to uniform illumination. We can take two types of flats, namely dome-flats and sky-flats. The two differ in the source of the illumination and the conditions under which they are taken. We take five dome-flats and five sky-flats in each of the Johnson-Kron-Cousins filters. Thus, the first fifty-five images on any night are bias frames, or flats.

We make dome-flat exposures in the afternoon with the dome closed. Three quartz halogen lamps operating at ~3000°C illuminate a specially prepared circular white background with a 0.9m diameter referred to as "Il punto blanco". While taking dome-flats, the color balanced filter is introduced into the optical path. The arrangement simulates the illumination of the 5500°C (Walker, 2000) night sky.

Following the acquisition of dome-flats, the telops opened the dome and turned on ventilation fans to ensure that the temperature in the dome matched that of the ambient environment. This improves the stability of the telescope focus, as the atmosphere and the air in the dome are all part of the optical path. The liquid nitrogen in the dewar surrounding the detector is also refilled.

The twilight sky is a uniform source of light. Flats taken using the zenith of the twilight sky as the source of illumination are called sky-flats. The telescope is "slewed" (i.e. its pointing is changed slightly) between frames in order to ensure that any stars that might appear in a frame can be removed by appropriately combining flats. Repeated surveys by CTIO personnel have not discovered any significant polarization effects (Walker, 2000). Sky-flats are preferred to dome-flats, as they use a natural source and appear to flatten data-frames better (Massey, 1997). Following the acquisition of sky-flats, the night's observing begins.

2.6 The Real Time Display and On-site Analysis

The real time display (RTD) at the 0.9-m telescope automatically removes the overscan and trims the image for display. In addition, every pixel that reports more than 65535 ADUs is colored red. Such pixels are called "hot." We examine each frame after acquisition to ensure that we have sufficient signal for target objects to perform reliable photometry. We also determine the full-width at half maximum (FWHM) of the point-spread function (PSF) of the object using the RTD. There is a tradeoff between acquiring sufficient signal and the amount of trailing caused by the object's non-sidereal motion, observed from a siderealy-tracked telescope. To maximize the height of the PSF, we need to integrate for a long time. However, the non-sidereal motion of the object causes an undesirable increase in the FWHM of the PSF (see Fig. 2.5). This is particularly significant for C/2002 CE$_{10}$ (LINEAR) and is discussed in section 2.8.
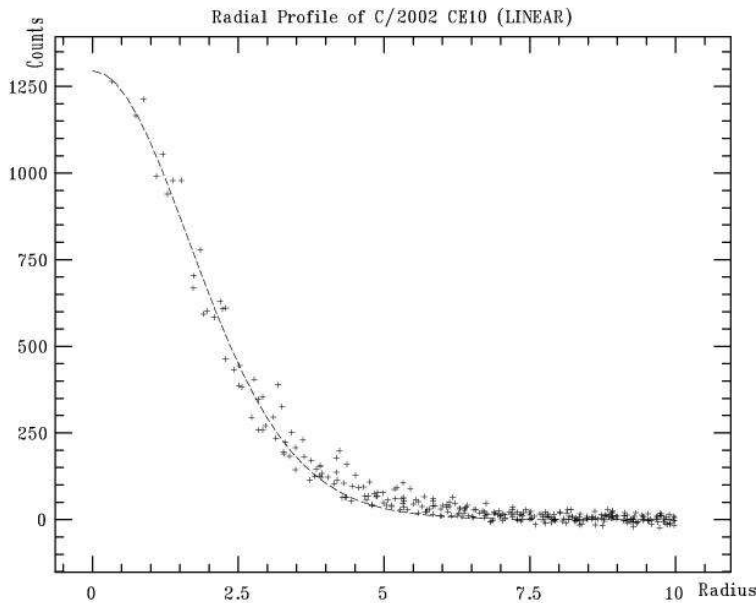
Figure 2.5: A typical radial profile of an outer-belt object plots the counts per pixel against the distance from the measured centroid of the object in pixels. The object in this case is C/2002 CE$_{10}$ (LINEAR). All pixels within a circular aperture of radius ten pixels, centered on the measured centroid are included in the scatter plot. The frame used to generate this plot has been processed using the procedure discussed in Chapter 3. Despite tracking non-siderealy at an estimate of the comet's speed in the sky, the FWHM is less than four pixels.

11

2.7 Observing Landolt Standard Stars

We observed several Landolt standard stars throughout the night at a range of airmass values to ensure that we could calibrate photometry for the entire night over a wide range of airmass values and magnitudes.

2.8 Observing Outer-belt Objects - Telescope Tracking Rates and Airmass

Integration times for outer-belt objects are considerably longer than for standards, as these are the targets of this study and their apparent magnitudes are considerably higher than standards (i.e. they are much fainter). As 279 Thule moved relatively slowly across the field, the telescope was tracked at the sidereal rate and we used the autoguider to correct the telescope pointing. The PSF of 279 Thule revealed very little broadening due to trailing, even for four minute integrations; thus, for photometric purposes, we can treat 279 Thule as a fixed-point object (see Fig. 2.6 below).

Figure 2.6: A typical contour plot of 279 Thule reveals very little broadening, or deviation from circularity, despite the difference between its motion across the sky and the sidereal tracking rate of the telescope. We produced this contour plot from a 240-second exposure, in the 'V' filter. Most integration times for 279 Thule were considerably shorter.
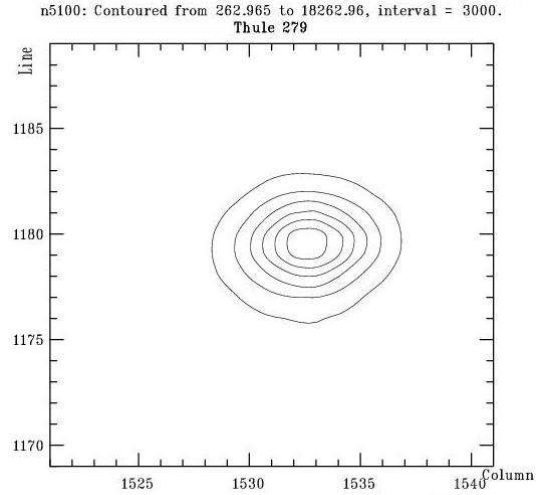
Tracking siderealy also allows us to compare 279 Thule's instrumental magnitude to instrumental magnitudes of stars in the same field. These "comparison star" instrumental magnitudes are assumed fixed. This process is known as "differential-photometry" and can be used to give a quick estimate of the magnitude variation of 279 Thule between frames.

Initially, we also tracked C/2002 CE_{10} (LINEAR) siderealy. This object did exhibit significant trailing. This was thought to be the result of near nucleus-comae that had been reported from the observations by the 8.2 m Subaru telescope discussed earlier. On the fourth night, we decided to track the telescope non-siderealy at the estimated speed of the object in the sky. This minimized the trailing of the object at the cost of trailed star images (see Fig. 2.7) and thus made differential photometry impossible. It was found that the trailing exhibited by C/2002 CE_{10} (LINEAR) was primarily the result of its rapid motion across the frame as the FWHM of its PSF was very comparable to 279 Thule when tracked siderealy. All photometry of C/2002 CE_{10} (LINEAR) is from the fourth night and onwards, from when we used the estimated non-sidereal speed of the object in the sky as the tracking rate of the telescope.
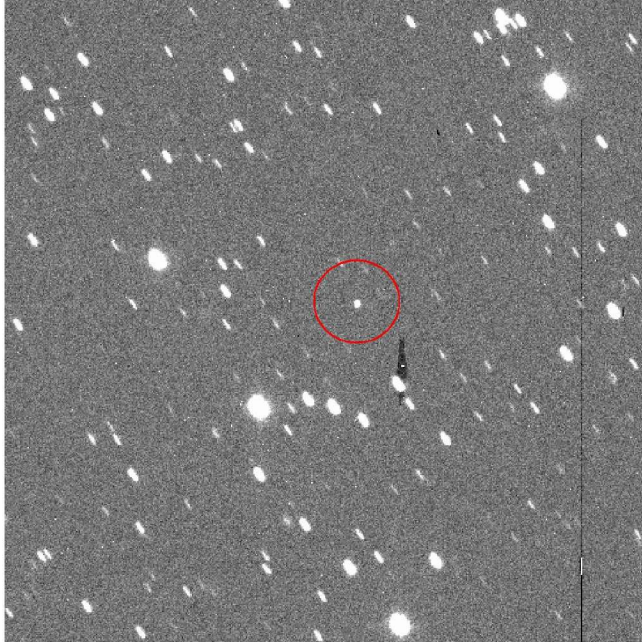
Figure 2.7: A section of a typical data frame of C/2002 CE$_{10}$ (LINEAR) processed using the procedure described in Chapter 3. Stars in the frame are trailed because of the non-sidereal tracking rate of the telescope, when observing the comet, which is the un-trailed object, circled near the center of the image. The dark region below and right of center and the dark column towards the right of image are caused by "hot" or damaged pixels. Such pixels occur near the edge of the CCD and these are trimmed. Those that occur well away from the edge cannot be removed and care is taken to ensure that target objects are not imaged by such damaged pixels. The radial profile in Figure 2.5 was generated from this frame.

Wherever possible, we observed target at an airmass of < 1.6; however, this constraint was occasionally relaxed to ensure sufficient lightcurve coverage. We do not use images taken at airmass' greater than 1.9 for photometry. ARCON calculates the airmass and automatically writes it to the data image headers. We monitored the weather on-site continuously. CTIO personnel used a separate telescope to monitor the FWHM of various stars near the zenith. This gives a measure of the stability of atmospheric conditions or "seeing" on-site.

2.9 End of Observing Procedures

We filled the dewar with liquid nitrogen at the end of the night's observing. At no point did we allow the temperature of the detector to rise above 90 Kelvin. It is standard procedure to cover the telescope in order to prevent dust settling on the primary overnight.

3. IMAGE REDUCTION

Before any analysis can occur, we "clean" the data to improve the SNR, using a set of procedures collectively called image reduction. Image reduction is a conceptually simple exercise, but is very time consuming and computationally intensive. We performed all image reduction using the Image Reduction and Analysis Facility (NOAO PC-IRAF v2.12) with the X11/IRAF v1.3 graphics extensions and the SAO DS9 display tool.

3.1 Overscan Correction and Trimming

First the overscan region generated by each of the four amplifiers must be removed from all the data and the separate regions read out by the amplifiers must be joined together to produce one complete frame. This process is known as "overscan subtraction." The overscan region is set in the ARCON software, which writes the address range of columns in the overscan region the image header.

Some of the pixels and columns near the edge of the frame are unusable because they are not illuminated or because of local defects, usually produced when the fused silica window is connected to the CCD. These pixels and columns always readout 65535 ADU and are therefore referred to as "hot." The response of pixels near hot pixels or columns is also suspect. Therefore, some columns and rows near the edge of the CCD are removed from every bias, flat and data frame. This process is called "trimming." The section of the image to be trimmed is left to the discretion of the observer unlike the overscan region, which is a detector characteristic.

We determined the region to be trimmed by making a plot of the average number of pixel level along ten rows of the CCD from a bias frame. Hot columns are evident from such a plot and we selected the region near the edge, which had a nearly constant bias level as the region to be retained. A nominal range for the trim section is determined by the telops and ARCON writes this range into the image header.

The overscan and trim region must be removed from bias frames, separately from flats and data frames. This is because in addition to overscan and trim correction, the bias level must also be removed from flats and data frames.

The option to remove the overscan and trim region can be defined by parameters in the IRAF task *quadproc* defined in the *noao>imred>quadred* package. A simple list of the bias frames for each night is created and passed to *quadproc*, which removes the overscan and trim region from each bias when the appropriate parameters are specified[3.1].

[3.1]In practice, *quadproc* splits a frame into its four separate regions and calls the *ccdproc* task, defined under *quadred*, on each of the regions individually. Based on the *quadproc* parameters, each of the regions can be trimmed, the overscan bias estimated, the overscan and bias subtracted, and flat-fielded by *ccdproc*.

3.2 Bias Correction

After trimming and overscan subtraction, the list of bias frames is passed to the IRAF task *zerocombine*, defined under *quadred*, to produce a "master bias" calibration frame, which is an average of the ten bias frames taken every night (see Fig. 3.1).
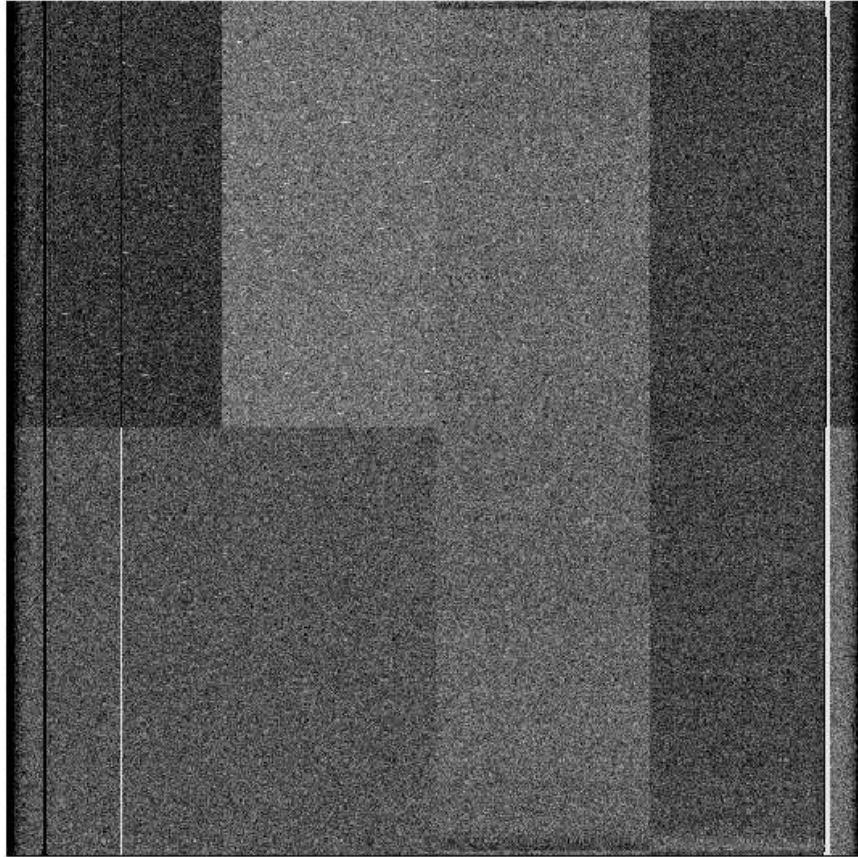

Figure 3.1: A typical master bias produced using the procedure described above. The display tool maps the slightly different electrical backgrounds to different shades of grey. A comparison to a raw frame such as Fig 2.1 reveals that the dark regions near the top and bottom of the frame have been trimmed and the overscan column near the center of the image has been subtracted and the four separate regions have been joined together by *quadproc*.

As discussed earlier, the bias level for each of the four regions is different and is found empirically to vary with column address, temperature and telescope position, among other factors. The bias level must therefore be dynamically determined for every flat and data frame. A list of all the flats is created and is passed to *quadproc*. An additional parameter specifying the path of the master bias file must also be set. Each flat is trimmed and the bias of every of every row is estimated from the overscan region which is then subtracted. The bias estimate from the overscan region and the master-bias calibration file is used to remove the bias from every pixel. From this point onwards, the level in ADU at each pixel is treated as a real number rather than an integer, to avoid introducing artificial rounding errors.

3.3 Flat-fielding

After trimming, overscan subtraction and bias removal, the list of flats is passed to the IRAF task *flatcombine*, also defined under *quadred*, to produce "master flats" for each of the Johnson-Kron-Cousins filters (see Fig. 3.2). Dome-flats and sky-flats are passed to *flatcombine* separately. Parameters specifying filter name, exactly as it appears in the image header information written by ARCON, must be set. The master flat for each filter is created by taking the median of the five flats in each of the corresponding filters. Taking the median causes small sources of noise such as cosmic rays, which will not be present in the same location in each of the flats, to be rejected. We did not find any large sources of noise, such as birds or airplanes, in any of the flats. We chose to use the master sky-flats in order to normalize the pixel response for the reasons detailed in the previous chapter.
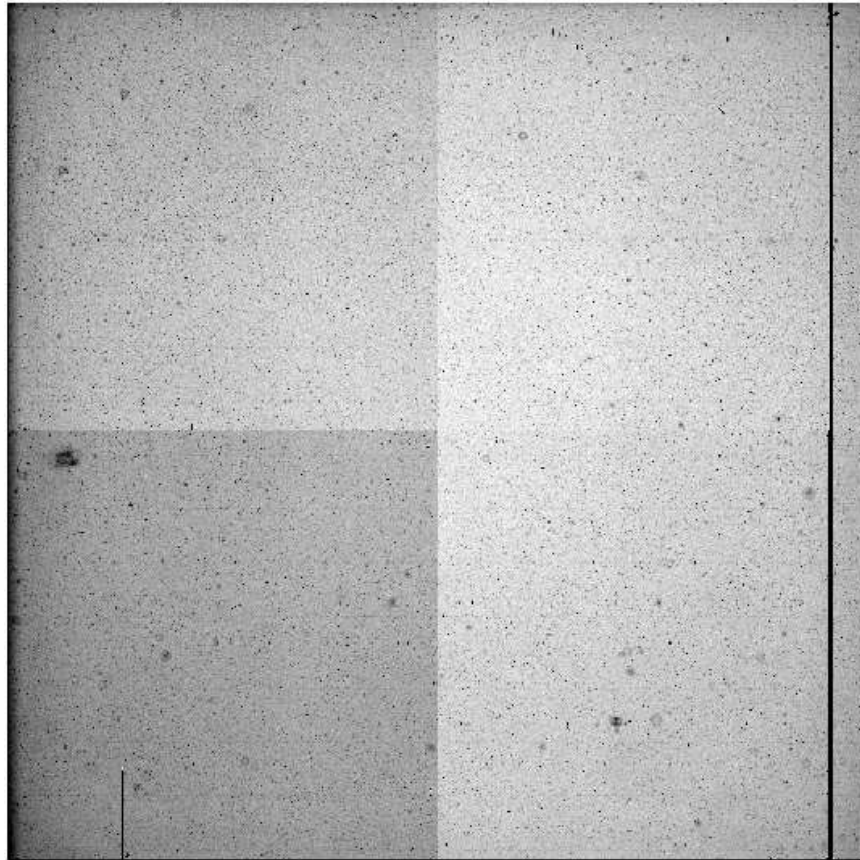
Figure 3.2: A typical master sky flat produced using the procedure described above. We took this sky flat in the 'V' filter. The section shown in Fig 2.4 is from the bottom right quadrant of this image. We removed the electrical background caused by the readout electronics by bias subtraction, using the master bias shown in Fig 3.1.

As discussed earlier, the response of pixels varies across the CCD and there are small and large-scale non-uniformities that arise from CCD fabrication, as well as localized non-uniformities arising from sources in the optical path. The response of each pixel must therefore be normalized for every data frame. A list of all the data images is created and is passed to *quadproc*. Additional parameters specifying the paths of the master flats and

filter name, exactly as it appears in the image header information written by ARCON must also be set. Each image is trimmed, the overscan subtracted and the bias corrected and the response normalized by dividing it by the master flat in the corresponding filter (see Fig. 3.3). Once the image has been flat-fielded, every pixel has a uniform response, and the level at one pixel can be compared to the level at another pixel. The level at each pixel is now referred to as the "counts" for the pixel.
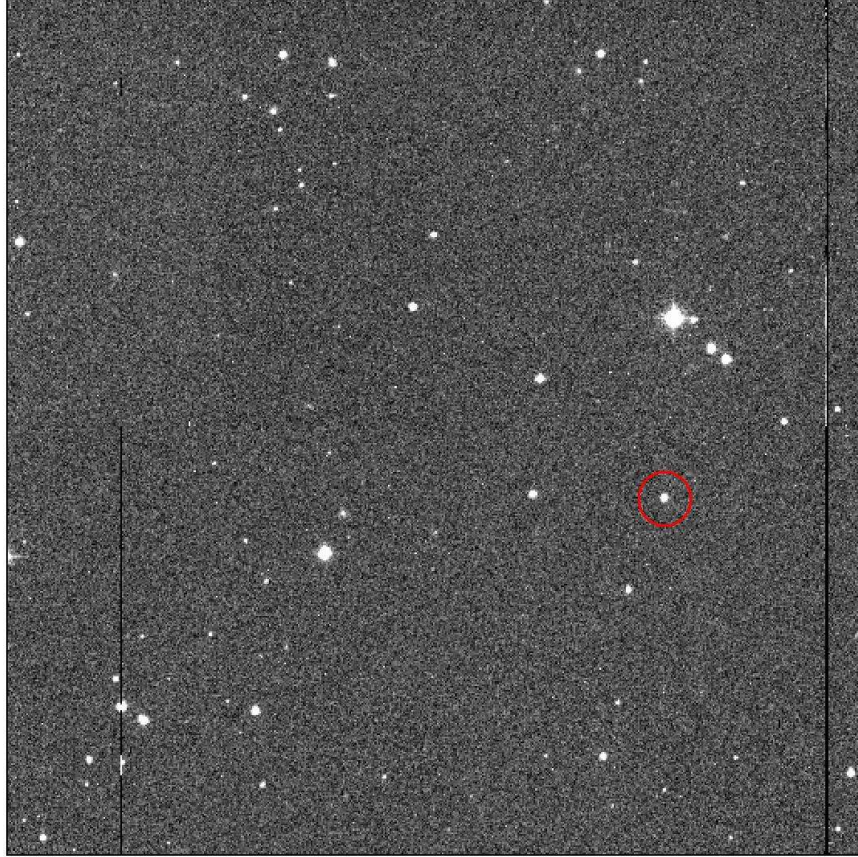
Figure 3.3: A typical frame after trimming, overscan subtraction, bias correction and flat fielding. We performed bias correction using the frame in Fig 3.1, and flat fielding using the frame in Fig 3.2. We took this image using an integration time of 240-seconds in the 'V' filter. The circled object in the figure is 279 Thule. We generated the contour plot of 279 Thule in Fig 2.6 from this image. This is the same frame as in Fig 2.1. The effect of image reduction is considerable and very apparent.

4. PHOTOMETRY

Following image reduction, we can extract instrumental magnitudes for all the objects. The instrumental magnitude is determined using the magnitude equation[4.1]

$$m_f = -2.5 \log(I_f) + Z_f \tag{4.1}$$

where the instrumental magnitude in filter 'f', 'm_f' is related to the measured intensity in that filter 'I_f' and some constant zero-point 'Z_f' for the filter to convert to some magnitude system. The zero-point is removed when we transform instrumental magnitudes to apparent magnitudes in the Johnson-Kron-Cousins system. We perform fixed circular aperture photometry to extract instrumental magnitudes for all objects of interest using the IRAF routine *phot* defined under noao>*digiphot*>*apphot*. There are several different configurations available for *phot* and we shall only discuss the ones that we used, that are standard for CCD photometry in uncrowded fields.

The counts from an object remain at a significant level for a large distance from its centroid. It has been shown that even when the FWHM is three pixels, corresponding to a radial profile that falls off rapidly, the increase of area with radius is high and therefore an increase in aperture size from 18 to 20 pixels can cause a 1-2% increase in the light from the star (Massey et al; 1989). Therefore, we can never measure all of the counts produced by any object. As there are always several stars in a frame, we do not get the counts caused by just the object of interest, but in addition the counts of the background sky. Thus, when doing fixed aperture photometry there is a tradeoff between using a larger aperture to get all the counts from the star and using a small aperture to minimize contamination from the background sky.

Ideally, every object of interest would have a circularly symmetric PSF but in practice, several factors contribute to the smearing of the PSF including telescope tracking rate errors, errors in the focus and especially errors caused by variability of atmospheric conditions on-site. The stability of atmospheric conditions on-site or "seeing" is measured using the FWHM of the PSF of near-zenith stars. Accurate photometry demands good seeing (i.e. that the FWHM be small) as well as that the region around the object of interest be free of other sources of light, which will allow us to estimate an average background level.

4.1 Centroid Determination, Background Removal & Aperture Photometry

We define parameters in *phot* that set the radius of a circular aperture around the centroid of the object and the width and inner radius of an annulus concentric with the aperture. *phot* uses pixels within the circular aperture to determine the instrumental magnitude and pixels within the annulus to estimate the level of background sky noise. The inner radius of the annulus must be strictly greater than the radius of the aperture, so that *phot* does not enumerate the same pixels for both intensity and background level. IRAF does not provide any tools with which to determine how the instrumental and background sky

---

[4.1] The magnitude equation is discussed in Appendix A.

level, vary with aperture size and we therefore performed aperture photometry with three nominal aperture sizes for observations at the CTIO 0.9-m telescope. We also define a template entry name that *phot* uses as the root entry name under which aperture photometry results are stored in a text file.

We display the frame in the DS9 display tool and call *phot*. The routine allows us to locate the approximate centroid of the target object on the frame. *phot* then uses the approximate centroid as an initial guess to determine the true centroid by computing the intensity weighted mean of the marginal intensity distributions of 'x' and 'y' separately. Using the pixels within the annulus, *phot* constructs a distribution of the intensity against the total number of pixels at that intensity and rejects those that are outside three standard deviations. The mode of the remaining pixels is determined and normalized to unit area. This is the measured background sky level per unit area, 'S_{Sky}'.

Finally, the routine performs aperture photometry by summing the counts of all the pixels entirely within the circular aperture. Pixels only partially inside the aperture are treated by approximating the fraction within the aperture and summing each of the approximations. The difference between the counts measured in the aperture 'N_{Aper}' and the product of the aperture area and sky background level per unit area 'S_{Sky}' is calculated. The difference is normalized to unit time and this intensity is used to calculate the instrumental magnitude (see Fig. 4.1).

The routine then writes out the determined location of the object's centroid and its associated error, the instrumental magnitude of the sky background and its error, the filter used for the frame, the instrumental magnitude in the filter and its error and other data, under a named entry based on the supplied template, to a file for the input data frame. If a frame contains more than one target object, such as a frame containing standard stars, we repeat the procedure sequentially on all the objects and *phot* appends results for each object to the same file, under different named entries. We repeat the process for every data frame and thus every frame has a separate file containing the instrumental magnitudes and other results of aperture photometry on objects within the frame (see Fig. 4.2). For frames of the same multiple object target fields, aperture photometry must be performed on each of the objects in exactly the same order throughout.
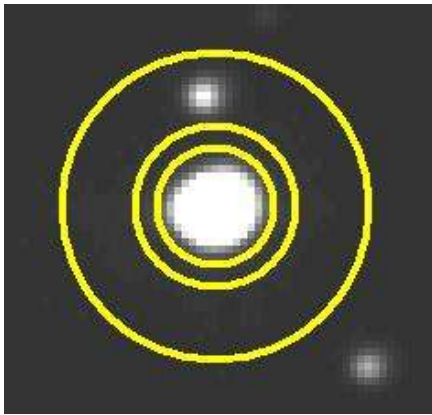
Fig 4.1: An illustration of how *phot* determines instrumental magnitudes. The centroid of the object is determined. A circular aperture of radius 12.5 pixels and an annulus of inner radius 15 pixels and width 10 pixels are drawn around the centroid. The sky fitting algorithim rejects all pixels that are considerable brighter than the background sky level. Thus, the star within the annulus in this image would not contribute to the sky background. The mode of counts per unit area is determined. The total number of counts within the aperture is determined, corrected using the level of the background sky and normalized to unit time. This number is used to determine the instrumental magnitude (using equation 4.1) which is written to file, along with other data. (Source: Bruce L. Gary, Hereford Arizona Observatory)

We used a magnitudes determined by aperture photometry with a circular aperture of radius 12.5 pixels and an annulus with inner radius 15 pixels and width 10 pixels.

```
#
#N IMAGE               XINIT    YINIT    ID   COORDS                LID   \
#U imagename           pixels   pixels   ##   filename              ##    \
#F %-23s               %-10.3f  %-10.3f  %-6d %-23s                 %-6d
#
#N XCENTER   YCENTER   XSHIFT   YSHIFT XERR   YERR            CIER CERROR  \
#U pixels    pixels    pixels   pixels pixels pixels          ##   cerrors \
#F %-14.3f   %-11.3f   %-8.3f   %-8.3f %-8.3f %-15.3f         %-5d %-9s
#
#N MSKY          STDEV        SSKEW        NSKY    NSREJ    SIER SERROR    \
#U counts        counts       counts       npix    npix     ##   serrors  \
#F %-18.7g       %-15.7g      %-15.7g      %-7d    %-9d     %-5d %-9s
#
#N ITIME         XAIRMASS     IFILTER               OTIME                 \
#U timeunit      number       name                  timeunit              \
#F %-18.7g       %-15.7g      %-23s                 %-23s
#
#N RAPERT  SUM         AREA       FLUX         MAG     MERR   PIER PERROR  \
#U scale   counts      pixels     counts       mag     mag    ##   perrors \
#F %-12.2f %-14.7g     %-11.7g    %-14.7g      %-7.3f %-6.3f %-5d %-9s
#
n5107                  1569.000 1195.000  1    nullfile            0       \
    1568.259  1195.416   -0.741 0.416   0.005  0.004            0   NoError \
    249.2101     12.35715      4.161094    1249    7            0   NoError \
    240.         1.449        diav                    06:12:47.000        \
    5.00     304247.8    78.82161   284604.7     17.315 0.002 0   NoError *\
    10.00    423798.8    314.4357   345438.2     17.105 0.002 0   NoError *\
    12.50    473720.6    490.9935   351360.      17.086 0.002 0   NoError *
```

Fig 4.2: Sample output from *phot*. The routine writes out the filter name, the computed centroid, the sky level and the computed magnitudes using all apertures, along with associated errors and other data to a text file.

4.2 Determining Coefficients of the Transformation Equation

The instrumental magnitude is dependent on the spectral response of the CCD, filter transmission properties and the atmospheric extinction. We remove these effects and convert to magnitudes in the Johnson-Kron-Cousins system using observations of faint stars in the Landolt catalog. The transformation equations[4.2] for the Johnson-Kron-Cousins BVRI system are

$$b = B + K_b + C_b (B{-}V) + E_b (X)$$
$$v = V + K_v + C_v (B{-}V) + E_v (X)$$
$$r = R + K_r + C_r (V{-}R) + E_r (X)$$
$$i = I + K_i + C_i (V{-}I) + E_i (X)$$

(4.2)

where lower case "$bvri$" stands for the instrumental magnitudes, upper case "$BVRI$" stands for magnitudes in the Johnson-Kron-Cousins system and 'X' is the average airmass during the observation. 'K_f' is a constant term; 'C_f' is the color term, while 'E_f' is the atmospheric extinction in the filter 'f' and we wish to determine these so that for any set of instrumental magnitudes '$bvri$', we can determine the corresponding '$BVRI$' magnitudes. 'K_f' and 'C_f' are characteristics of the filters and CCD. 'E_f' is often found to be a seasonal characteristic of the observing site. As the transformation equations depend on colors in two filters, they must be solved simultaneously. We define the equations in a text file.

[4.2] The transformation equations are discussed in Appendix A.

We use the instrumental magnitudes we previously measured for the standard stars, their magnitudes as measured by Landolt and the calculated airmass to determine the fitting parameters 'K_f', 'C_f' and 'E_f' for each filter. We create a list of the files output by *phot* from aperture photometry on Landolt standard star frames, in the different filters. We match observations in the different filters of the same field that are close in time and therefore airmass. Thus, in effect, we have multiple sets of instrumental '`bvri`' magnitudes for each standard star with Landolt's '`BVRI`' magnitudes at several different values of airmass.

We use the IRAF routine *mkobsfile* defined under *noao>digiphot>photcal*, to parse the list of matched standard star field observations and extract entry name, filter name, instrumental magnitude, error in measured instrumental magnitude, centroid position and associated error and airmass for each of the objects in each of the filters (see Fig. 4.3). This would not have been possible unless we had performed aperture photometry on each of the standard stars in exactly the same order, as *mkobsfile* would have attempted to match the instrumental magnitudes of different objects in different filters. IRAF prevents this by comparing the centroid positions of each of the standard stars in each filter. In addition, we crosschecked extracted centroid positions for each standard star, with the actual position of the star in the image frame, to ensure that they were indeed the same object. We then edit the generated entry names of the standard stars to match their names as given in the Landolt catalog. Catalog entries for Landolt standards used to calibrate photometry are given in Table 4.1.

TABLE 4.3: LANDOLT STANDARDS USED FOR PHOTOMETRY (Source: Landolt, 1992)

| Star | RA(2000) | Dec(2000) | V | B-V | V-R | V-I | n | m | Mean Errors of the Mean | | | |
									V	B-V	V-R	V-I
TPHE A	00:30:09	-46 31 22	14.651	0.793	0.435	0.841	29	12	0.0028	0.0046	0.0019	0.0032
TPHE C	00:30:17	-46 32 34	14.376	-.298	-.148	-.360	39	23	0.0022	0.0024	0.0038	0.0149
TPHE D	00:30:18	-46 31 11	13.118	1.551	0.849	1.663	37	23	0.0033	0.0030	0.0015	0.0030
TPHE E	00:30:50	-46 24 36	11.630	0.443	0.276	0.564	34	8	0.0017	0.0012	0.0007	0.0019
93 317	01:54:38	+00 43 00	11.546	0.488	0.293	0.592	37	28	0.0007	0.0008	0.0007	0.0008
93 333	01:55:05	+00 45 44	12.011	0.832	0.469	0.892	38	28	0.0015	0.0018	0.0010	0.0016
94 251	02:57:46	+00 16 02	11.204	1.219	0.659	1.247	52	45	0.0010	0.0014	0.0009	0.0011
95 132	03:54:51	+00 05 21	12.064	0.448	0.259	0.545	33	27	0.0023	0.0021	0.0016	0.0026
95 137	03:55:04	+00 03 33	14.440	1.457	0.893	1.737	1	1	...	...	...	...
95 139	03:55:05	+00 03 13	12.196	0.923	0.562	1.039	3	2	0.0017	0.0046	0.0023	0.0035
95 142	03:55:09	+00 01 19	12.927	0.588	0.588	0.745	22	11	0.0030	0.0030	0.0013	0.0028
95 218	03:54:50	+00 10 08	12.095	0.708	0.708	0.767	20	10	0.0034	0.0022	0.0020	0.0027
95 190	03:53:13	+00 16 20	12.627	0.281	0.195	0.415	44	22	0.0020	0.0017	0.0017	0.0021
95 193	03:53:20	+00 16 31	14.338	1.211	0.748	1.366	20	10	0.0049	0.0063	0.0042	0.0058
98 650	06:52:05	-00 19 40	12.271	0.157	0.080	0.166	31	20	0.0020	0.0014	0.0016	0.0027
98 653	06:52:05	-00 18 19	9.539	-.004	0.009	0.017	65	50	0.0014	0.0004	0.0007	0.0011
98 670	06:52:12	-00 19 17	11.930	1.356	0.723	1.375	32	19	0.0016	0.0018	0.0018	0.0023
98 671	06:52:12	-00 18 22	13.385	0.968	0.575	1.071	27	15	0.0037	0.0048	0.0033	0.0046
98 675	06:52:14	-00 19 41	13.398	1.909	1.082	2.085	44	21	0.0026	0.0035	0.0018	0.0024
98 676	06:52:14	-00 19 21	13.068	1.146	0.683	1.352	17	8	0.0032	0.0041	0.0015	0.0032
98 682	06:52:17	-00 19 42	13.749	0.632	0.366	0.717	13	7	0.0039	0.0039	0.0017	0.0039
98 685	06:52:19	-00 20 19	11.954	0.463	0.290	0.570	22	14	0.0030	0.0021	0.0023	0.0034
MARK A1	20:43:58	-10 47 11	15.911	0.609	0.367	0.740	25	10	0.0040	0.0090	0.0044	0.0148
MARK A2	20:43:54	-10 43 52	14.540	0.666	0.379	0.751	21	10	0.0028	0.0031	0.0024	0.0059
MARK A3	20:44:02	-10 45 39	14.818	0.938	0.587	1.098	22	10	0.0023	0.0034	0.0021	0.0045

RA= right ascension   Dec = declination   V=mean apparent visual magnitude   B-V, V-R, V-I = mean color indices
n = # of separate nights that standard was observed   m = # of separate times that standard was observed

We pass the output of *mkobsfile* to the IRAF task, *fitparams* also defined under *noao>digiphot>photcal*. The Landolt catalog is used so routinely that it is included in every IRAF installation. The text file with the defined transformation equations is also passed to *fitparams*. The routine parses the input file for instrumental magnitudes and errors, as well as airmass and matches these to the corresponding magnitudes of the standard star as given in the Landolt catalog. The routine then uses a least squares fitting routine to determine the fitting parameters, 'K_f', 'C_f' and 'E_f', for each filter simultaneously. The task is interactive in that it allows the user to delete data points and create different views (see Fig. 4.4). Data points deleted from one fit are automatically removed from all other fits. The routine outputs the values of the fitting parameters for each filter and their associated errors, to an output file.

It was not possible to fit the transformation equations on the first night of observing (2003 Oct 14) without deleting several standards. The fitting parameters were found to be very different from those obtained on all other observing nights and their associated errors were significantly higher than the mean error. This is indicative of non-photometric conditions and therefore we reject all data from the night. Mean transformation coefficients for the filters used in photometry of 279 Thule and C/2002 CE$_{10}$ (LINEAR) are given in Table 4.2.

```
95_137          diav    8:03:01.0  1.214   962.326  1449.063  16.879  0.005
*               diai    8:10:41.0  1.227   963.053  1447.083  15.968  0.003
*               diar    8:08:53.0  1.224   962.615  1449.095  16.029  0.004
95_139          diav    8:03:01.0  1.214   927.114  1495.929  14.610  0.001
*               diai    8:10:41.0  1.227   927.896  1493.860  14.418  0.001
*               diar    8:08:53.0  1.224   927.323  1496.000  14.089  0.001
95_142          diav    8:03:01.0  1.214   750.721  1762.919  15.345  0.002
*               diai    8:10:41.0  1.227   751.538  1760.754  15.424  0.002
*               diar    8:08:53.0  1.224   750.904  1763.030  14.999  0.002
```

Figure 4.3: A section of the output generated by *mkobsfile*, when called on a list of matched standards. We edited the list so that the name of the entries matches the names of the corresponding stars in the Landolt catalog. The remaining columns contain the filter names, observation times, airmass, x and y positions of the object on the frame, measured instrumental magnitude and associated error. Note that the three sets of standards have "VRI" observations carried out at the same time and airmass in each filter. This indicates that the same field was observed in each filter and each frame contains at least these three standards. The output from *mkobsfile* when called on all frames containing standards collected during a nights observing spans several pages.

Table 4.4: MEAN TRANSFORMATION COEFFICIENTS

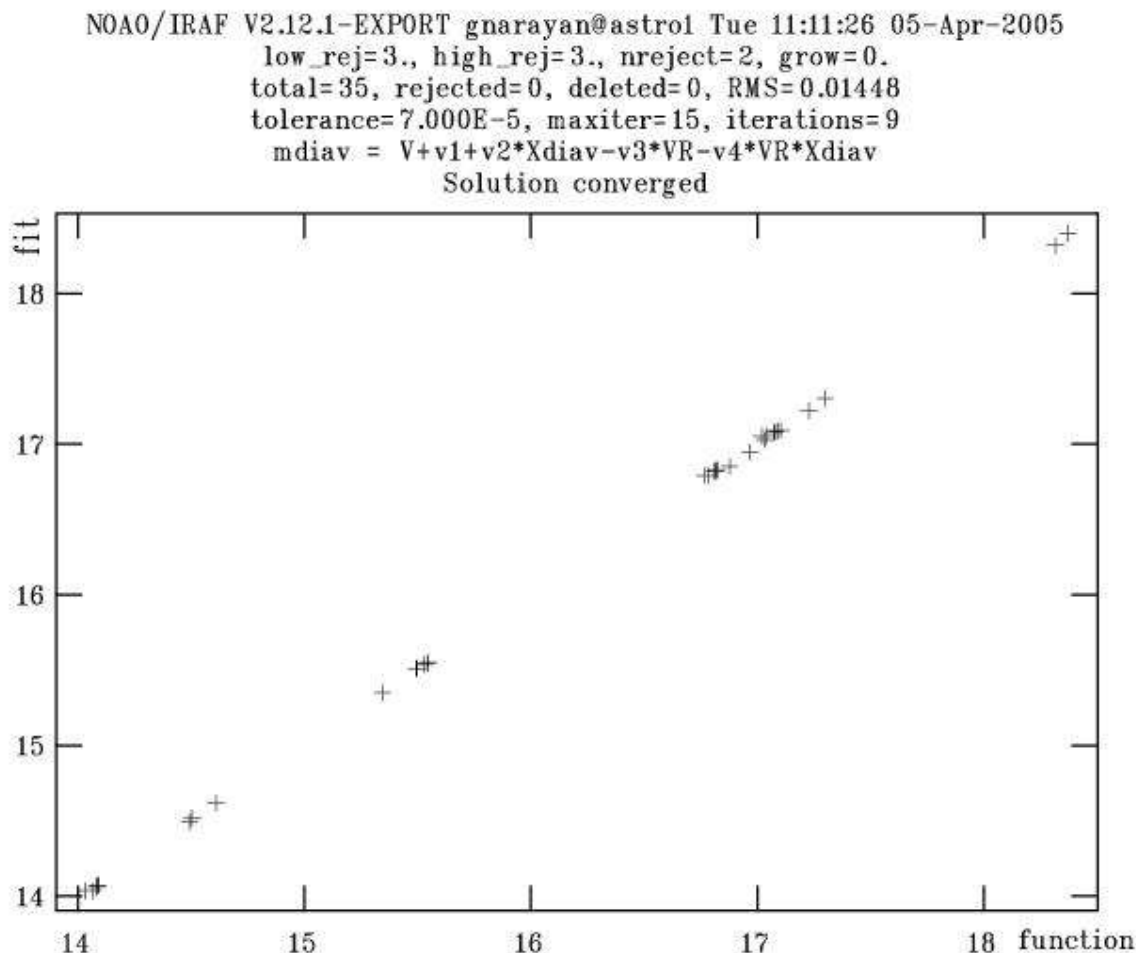| Filter	Zero Point	Extinction	Color
V	2.29 ± 0.04	0.12 ± 0.03	0.02 ± 0.01
R	2.34 ± 0.02	0.08 ± 0.02	0.01 ± 0.01

Figure 4.4: A typical result from *fitparams*. This particular result is from solving the transformation equation for the visual magnitude 'V' in the Landolt system. Thirty-five standard star observations at various values of airmass, are taken at different times throughout the night in each of the different filters. We reduced the frames with these objects as described in Chapter 3 and then performed aperture photometry on each of these 35x4 =140 standards. We created a list of matched observations and various datum extracted by *mkobsfile*. We executed *fitparams* which determined the coefficients in the transformation equations using the Levenberg-Marquardt least-squares algorithm. The status on top of the fit tells us that the solution converged in nine of the 15 allowed iterations when the convergence tolerance, or fractional change in chi squared from iteration to iteration, became less than the allowed 7e-5. *fitparams* determined a solution without rejecting a single data point, or requiring us to delete any manually. The routine also displays the RMS error of the fitting parameters.

We create a list of the files output by *phot* from aperture photometry on outer-belt objects in the different filters. We match observations in the different filters of the same field that are close in time and therefore airmass. We use the IRAF routine *mknobsfile* defined under *noao>digiphot>photcal* to parse the list of matched outer-belt object observations and extract entry name, filter name, instrumental magnitude, error in measured instrumental magnitude, centroid position and associated error and airmass for each of the objects in each of the filters (see Fig. 4.5). We can invert the transformation equations, and using the coefficients determined by photometric calibrations onto the Johnson-Kron-

Cousins system using faint stars observed by Landolt, we determine the apparent magnitude of the object.

# FIELD	FILTER	OTIME	AIRMASS	XCENTER	YCENTER	MAG	MERR
Thule1	diar	3:48:42.0	1.210	1432.072	1138.275	16.672	0.001
*	diav	3:54:23.0	1.209	1437.009	1142.439	17.093	0.002
Thule2	diar	4:00:08.0	1.208	1442.237	1145.745	16.674	0.001
*	diav	4:05:39.0	1.208	1447.004	1147.173	17.089	0.002
Thule3	diar	4:11:05.0	1.209	1452.459	1148.565	16.667	0.001
*	diav	4:16:07.0	1.211	1456.517	1150.452	17.088	0.002
Thule4	diar	4:21:08.0	1.213	1461.583	1152.353	16.661	0.001
*	diav	4:26:10.0	1.215	1465.490	1153.755	17.088	0.002
Thule5	diar	4:31:07.0	1.219	1470.492	1155.210	16.681	0.001
*	diav	4:36:11.0	1.223	1474.526	1156.519	17.080	0.002
Thule6	diar	4:41:10.0	1.227	1479.677	1158.551	16.664	0.001
*	diav	4:46:15.0	1.232	1483.557	1160.617	17.084	0.002
Thule7	diar	4:51:23.0	1.238	1488.977	1161.556	16.662	0.001
*	diav	4:56:26.0	1.245	1492.953	1163.580	17.087	0.002
Thule8	diar	5:02:21.0	1.254	1498.596	1165.950	16.669	0.001
*	diav	5:07:20.0	1.262	1502.703	1167.052	17.086	0.002
Thule9	diar	5:32:38.0	1.315	1532.583	1179.534	16.661	0.001
*	diav	5:38:37.0	1.331	1537.618	1181.913	17.087	0.002
Thule10	diar	5:44:07.0	1.346	1543.391	1185.272	16.663	0.001
*	diav	5:49:34.0	1.363	1547.375	1187.280	17.088	0.002
Thule11	diar	5:55:14.0	1.382	1553.175	1188.547	16.663	0.001
*	diav	6:01:25.0	1.404	1557.777	1191.680	17.080	0.002
Thule12	diar	6:07:12.0	1.426	1563.766	1193.683	16.664	0.002
*	diav	6:12:47.0	1.449	1568.259	1195.416	17.086	0.002

Figure 4.5: A section of the output generated by *mknobsfile*, when called on a list of matched object images, in this case images of 279 Thule. There are 12 sets of matched observations in two filters each; therefore 24 images went into the making of this list. The output is identical to that generated by *mkobsfile* and the remaining columns contain filter names, observation times, object coordinates, measured instrumental magnitude, the associated error and airmass. Notice that the x and y position of the object steadily changes as time increases, indicating that the object is moving. This is a set of observations carried out over more than two hours.

4.3 Determining Magnitudes in the Johnson-Kron-Cousins System

The IRAF routine *invertfit*, defined under *noao>digiphot>photcal*, accepts the text file with the defined transformation equations, the output of *fitparams* containing the determined fitting parameters and errors and the output of *mknobsfile* with the matched instrumental magnitudes of the outer-belt objects in each of the filters and the airmass. It solves the transformation equations simultaneously with the determined fitting coefficients and instrumental magnitudes in each filter to get the apparent magnitudes in the Johnson-Kron-Cousins system, which it outputs along with the computed errors and entry name to a text file (see Fig. 4.6). The apparent magnitudes are not corrected for the object's changing heliocentric distance, geocentric distance and solar phase angle. They are simply the observed magnitude of the object in the Johnson-Kron-Cousins system.

```
# Sun 15:58:50 23-Jan-2005
# List of observations files:
#           outthulemag
# Config:   thuleconfig.cfg
# Parameters:      ctio.ans
#
# Computed indices for program and standard objects
#
# Columns: |
#      1       object id
#      2       V
#      3       error(V)
#      4       VR
#      5       error(VR)


Thule1     14.672  0.002   0.445   0.002
Thule2     14.668  0.002   0.438   0.002
Thule3     14.667  0.002   0.444   0.002
Thule4     14.666  0.002   0.450   0.002
Thule5     14.657  0.002   0.421   0.002
Thule6     14.660  0.002   0.442   0.002
Thule7     14.662  0.002   0.447   0.002
Thule8     14.658  0.002   0.438   0.002
Thule9     14.651  0.002   0.445   0.002
Thule10    14.648  0.002   0.443   0.002
Thule11    14.635  0.002   0.433   0.002
Thule12    14.636  0.002   0.437   0.003
```

Figure 4.6: A section of the output generated by *invertfit*, when called on the defined transformation equations, with the fitting parameter results from *fitparams* and the output of *mknobsfile*. The transformation equations are inverted and solved simultaneously to give the apparent visual magnitude, colors and associated errors for the object. The results are for the same data shown in Fig 4.4 using the all transformation equation parameters for the night. The 'V' parameters were determined in the fit of standard magnitudes using the 'V' transformation equation in Fig 4.3.

We then use the entry name to determine which set of matched observations produced, which set of output magnitudes and manually append an observation time for each set of observations. We take the observation time to be the time the shutter opened when we made an observation in the 'V' filter. This time is measured and output by ARCON as described in Chapter 2 and is contained in the image header under the keyword 'UTSHUT.' Using these observations times, we can determine the object's geocentric distance 'Δ', heliocentric distance 'r' and solar phase angle 'α' during the observation by generating ephemeris using the International Astronomical Union (IAU) ephemeris service for asteroids and comets at the Minor Planet Center (MPC).

4.4 Determining Absolute Magnitudes

The brightness of the object varies with the inverse square of the geocentric distance and the heliocentric distance therefore we can normalize measurements to a constant heliocentric and geocentric distance of 1AU, similar to the manner by which apparent magnitudes are converted to absolute magnitudes normalized to 10 parsecs. If 'V (r,Δ,α)' is the apparent visual magnitude dependent on heliocentric distance 'r', geocentric distance 'Δ' and solar phase angle 'α' and '$V(1,1,\alpha)$' is the magnitude corrected for variation of geocentric and heliocentric distance then the two magnitudes can be related using the magnitude equation and the inverse-square law by

$$V(1,1,\alpha) = V(r,\Delta,\alpha) - 5\log(r\Delta) \qquad (4.3)$$

This relation is valid for objects that are not strongly self-luminous and "shine" because of sunlight they reflect. We need to remove the effects of the changing solar phase but without prior knowledge of an object's shape and surface properties, it is impossible to determine the actual phase relation and even approximate phase relations are model dependent. The International Astronomical Union (IAU) Commission 20 adopted a phase relation based on the model first introduced by Lumme and Bowell (1981) as the standard relation to correct for solar phase angle in 1985 (Marsden, 1986). The adopted phase relation included functions determined empirically by observations of both low-albedo and high-albedo asteroids. The solar phase correction '$P(\alpha)$' (Bowell et al; 1989) is given by

$$P(\alpha) = -2.5\log[(1-G)\Phi_1(\alpha) + G\Phi_2(\alpha)] \qquad (4.4)$$

where 'G' is empirically determined to be 0.15. The adopted phase relation defines the functions '$\Phi_1(\alpha)$' and '$\Phi_2(\alpha)$' as

$$\Phi_1(\alpha) = \exp[-3.33(\tan(\tfrac{\alpha}{2}))^{0.63}]$$

$$\qquad (4.5)$$

$$\Phi_2(\alpha) = \exp[-1.87(\tan(\tfrac{\alpha}{2}))^{1.22}]$$

where the functions were determined empirically by observations of low-albedo asteroids and high-albedo asteroids respectively. As the solar phase correction '$P(\alpha)$' is dependent only on the solar phase angle 'α', the value of solar phase correction is available in lookup tables. A plot of the function is shown below.
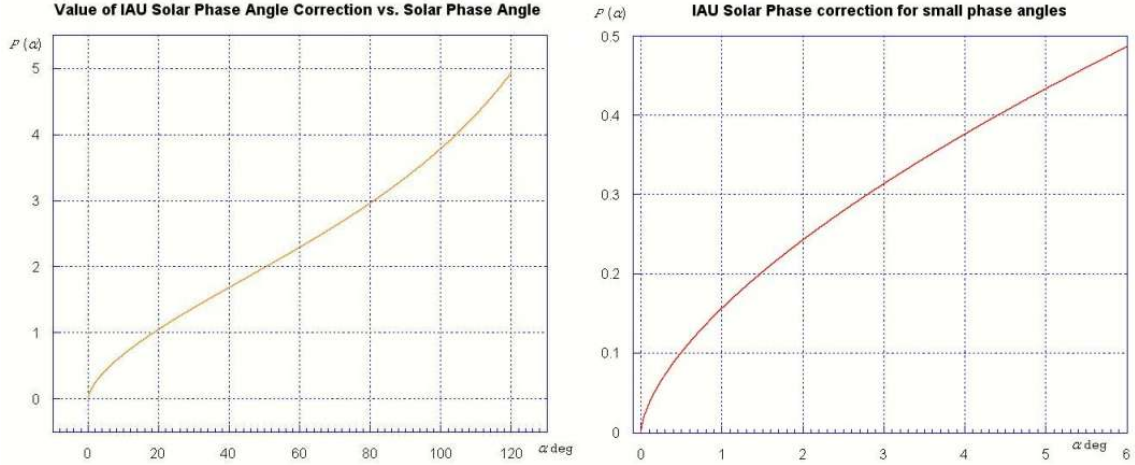
Figure 4.7: A plot of the solar phase correction, '$P(\alpha)$'. The solar phase relation is non-linear below 5 degrees and becomes significantly non-linear again above 100 degrees. The phase relation was empirically determined by studying 74 asteroid phase curves, Mercury, the Moon and other objects (Bowell et al; 1989).

We obtain absolute magnitudes from '$V(1,1,\alpha)$' using

$$V(1,1,0) = V(1,1,\alpha) - P(\alpha) \tag{4.6}$$

where '$V(1,1,0)$' is the absolute magnitude i.e. the apparent visual magnitude '$V(r,\Delta,\alpha)$' normalized to a geocentric and heliocentric distance of 1AU and zero phase angle. The apparent magnitude can be expressed in terms of the absolute magnitude using the above equations as

$$V(r,\Delta,\alpha) = V(1,1,0) + 5log(r\Delta) + P(\alpha) \tag{4.7}$$

Several asteroids exhibit a non-linear decrease in the apparent magnitude as the solar phase angle approaches zero (i.e. as the object approaches opposition). The object therefore appears significantly brighter near opposition. This marked change in the apparent magnitude, when the object is near $\alpha=0$ is known as the opposition effect. The solar phase correction based on the model of Lumme and Bowell using the empirically determined adopted by the IAU is appropriate for many asteroids and includes the opposition effect. The solar phase correction is zero for zero phase angle and increases non-linearly with increase in phase angle while the phase angle is small (see Fig. 4.7). However, there are asteroids that do not exhibit an opposition effect (French, L.M. 1987).

5. ANALYSIS AND RESULTS

5.1 Period Determination Using Phase Dispersion Minimization

As the outer-belt object rotates about an internal axis, the amount of light it reflects, and therefore its absolute magnitude, is a periodic function of time. We do not have continuous measurements of magnitude with time, but rather measurements of the magnitude at different times. We use the phase dispersion minimization (PDM) algorithm developed by Stellingwerf (1978), to determine possible rotation periods of 279 Thule.

If the data consists of 'N' observations (i.e. $i = 1, 2, 3,\ldots, N$) of the magnitude 'x' with mean

$$\bar{x} = \frac{\sum_{i=1}^{N} x_i}{N} \tag{5.1}$$

where the ith observation is represented by the magnitude 'x_i' determined at some time 't_i'. The variance 'σ^2' of the magnitude 'x' is

$$\sigma^2 = \frac{\sum_{i=1}^{N} (x_i - \bar{x})^2}{N - 1} \tag{5.2}$$

The algorithm divides the data into 'M' (i.e. $j = 1, 2, 3,\ldots, M$) distinct bins with the jth bin containing 'n_j' data points picked such that they have similar values for the rotational phase 'ϕ_i', determined assuming some rotational period 'Π' such that

$$\phi_i = t_i \ mod(\Pi) \tag{5.3}$$

If the jth bin containing 'n_j' data points has a bin variance denoted by 's_j^2', computed in exactly the same manner as the variance for the 'N' data points, then the overall variance of all the samples, 's^2' is

$$s^2 = \frac{\sum_{j=1}^{M} (n_j - 1) s_j^2}{\sum_{j=1}^{M} n_j - M} \tag{5.4}$$

The algorithm defines the statistic 'Θ' as the ratio of the overall variance to the variance of the magnitude 'x'

$$\Theta = \frac{s^2}{\sigma^2} \tag{5.5}$$

The algorithm repeats the procedure for several trial periods 'Π', and determines the minimum value of 'Θ'. The statistic is minimized when the overall variance of the bins 's^2' is minimized. This corresponds to when the trial period 'Π' is close to the true period as when this condition is met, data from each bin are from the same region of the true

lightcurve, and therefore have the same rotational phase. Consequently, the variance of each bin 's_j^2' is minimized.

PDM is the standard method to determine the rotation periods of object whose lightcurve has been discretely sampled at different rotational phases. IRAF therefore includes an implementation of the PDM algorithm, using the *pdm* routine defined under *noao>astutil* package. The routine accepts a list of absolute magnitudes, associated errors and the observation times that correspond to the absolute magnitudes. The routine then searches for the period that minimizes 'Θ' within a range of periods defined by the user, and outputs the results graphically.

5.2 The Magnitude Equation and Size Ratios

Using the observed difference in the absolute magnitude of the lightcurve, we can place a lower limit on the ratio of the comet's dimensions using the magnitude equation

$$M_A - M_B = -2.5 \log \left(\frac{I_A}{I_B} \right) \tag{5.6}$$

where '$M_A - M_B$' is the difference between the observed minimum and maximum absolute magnitude, and 'I_A' and 'I_B' are the intensities that correspond to the observed minimum and maximum magnitude. The observed intensity is proportional to the area that the object presents towards the earth and therefore

$$M_A - M_B = -2.5 \log \left(\frac{S_A}{S_B} \right) \tag{5.7}$$

where 'S_A' and 'S_B' are the surface areas presented towards the earth. Furthermore, if we assume that the surface area presented towards the earth is the projection of a spherical object onto a plane, then the surface areas S_A and S_B are given by the standard formula for the area of a circle, with diameters 'l_A' and 'l_B' respectively.

$$M_A - M_B = -5 \log \left(\frac{l_A}{l_B} \right) \tag{5.8}$$

While we cannot extract the actual dimensions of the object using this technique, we can combine it with radio observations of the object by the Infrared Astronomical Satellite (IRAS) to give some sense of scale for the object.

5.3 Results

The results of photometric analysis are given in Table 5.1. Instrumental magnitudes were determined after the data was bias corrected and flat-fielded, using aperture photometry with a 12.5 pixel radius circular aperture. We transformed instrumental magnitudes into the Johnson-Kron-Cousin system using photometric calibrations of faint stars observed by Landolt (1992), are given in Table 5.1.

TABLE 5.1: RESULTS

Object	$V(r,\Delta,\alpha)$	$V(1,1,0)$	$V-R$	Size ratio
279 Thule	14.66 ± 0.01	8.66	0.44 ± 0.03	1.26:1
C/2002 CE$_{10}$	$17.57^* \pm 0.01$	13.11^*	$0.54^* \pm 0.02$	–

* likely contamination by coma makes these results suspect

5.4 Results for 279 Thule

We observed 279 Thule on six nights (2003 Oct 14 and Oct 16 – 20) at solar phase angles between 1.5 and 2.5 degrees with the telescope tracked at the sidereal rate. All data from the first night of observing (2003 Oct 14) is rejected as conditions were not photometric.

The object's apparent sky motion is small and we do not believe that tracking at the sidereal rate introduced any significant errors. We find the object has a mean absolute magnitude of 8.66±0.02. This absolute magnitude was computed using the phase relation adopted by IAU as standard. The absolute magnitude was found to decrease over the observing run as the solar phase angle increased (see Fig. 5.1). This trend might be an artifact of imaging a different section of the lightcurve each night. If our observations sampled a section of the lightcurve that was lower in magnitude, than the section sampled the previous night then it would account for the trend. This would imply a rotational period that is less than sub-multiples of 24 hours. If this is the case, then no further analysis of the trend can be done.

However, the trend might also be caused by the IAU standard solar phase correction relation '$P(\alpha)$' defined in Bowell et al. (1989) being an ill-suited phase relation for 279 Thule. If the phase correction '$P(\alpha)$' increases too rapidly with phase angle, then the calculated absolute magnitude decreases with increase in phase angle. This artificial brightening with increase in phase angle would be an entirely unphysical effect, and a different phase relation for 279 Thule would be required.

The above scenario is given more credence by observations of objects similar to 279 Thule by French (1987), which do not exhibit an opposition effect. The L5 Trojans 1173 Anchises and 2674 Pandarus that were found not to exhibit an opposition effect have been classified as either C or P, and D type asteroids respectively; 279 Thule has been classified as a D type asteroid. All of these families are redder than most outer-belt asteroids. As discussed earlier, the IAU phase relation based on the Lumme and Bowell model, contains empirically determined functions that match the behavior of several low-

albedo and high-albedo asteroids that exhibit an opposition effect. The difference between the colors of C, D and P type asteroids and other outer-belt objects suggests that these asteroids have different surface properties than other outer-belt objects, especially those that are adequately explained by the IAU phase relation. The observations by French show that at least some asteroids obey a different phase relation than the one given by Bowell et al. (1989).
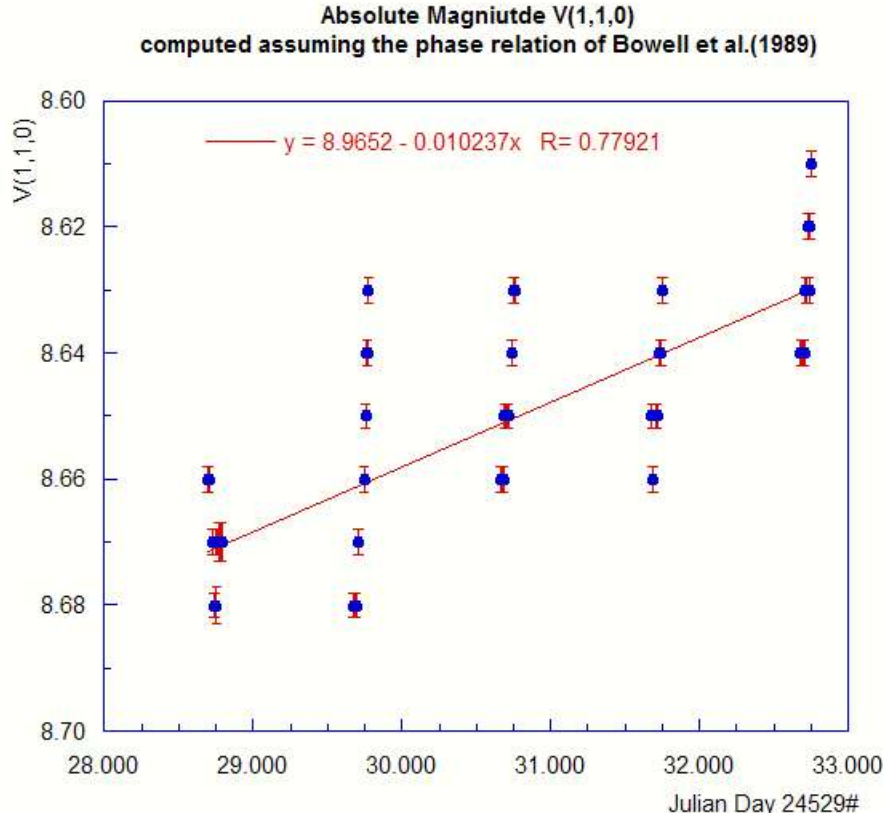

Figure 5.1: Absolute magnitudes, with computed errors in the apparent magnitude from each night. The absolute magnitudes show a decreasing trend (the vertical axis is inverted) corresponding to increasing brightness. The vertical scatter within each night is due to the asteroid rotation. A best-fit line is added to highlight this trend and has no physical meaning. The trend might be an artifact of sampling a different region of the lightcurve each night. In particular, if we sampled a section of the lightcurve that was at a lower average magnitude than the previous night's section then it would account for the decreasing trend in magnitude. The trend might also be accounted for by the IAU standard solar phase correction being unsuitable for objects that do not exhibit an opposition effect. We cannot conclusively exclude this possibility, which is indeed the case for some asteroids (French, L.M., 1987).

As we observed 279 Thule near opposition, we can carry this analysis further. If the Lumme and Bowell model is accurate for the object, then as we are moving away from opposition the apparent magnitude as a function of solar phase angle should show a non-linear increase, corresponding to a drop in brightness. A plot of the apparent magnitude dependent on solar phase angle '$V(1,1,\alpha)$' does increase with solar phase angle (see Fig. 5.2). We assume a linear phase relation to convert from apparent magnitude dependent on solar phase angle to absolute magnitudes i.e.

$$P(\alpha) = \alpha\beta \tag{5.9}$$

$$V(1,1,0) = V(1,1,\alpha) - \alpha\beta \tag{5.10}$$

as a consequence of equation 4.6. A best fit for '$V(1,1,\alpha)$' as a linear function of the solar phase angle reveals that the decrease in magnitude can be linear. We do not have sufficient coverage of the solar phase angle to rule out a non-linear decrease. If we could determine the shape of the lightcurve from Fourier analysis, we could normalize the apparent magnitudes to remove the rotational component of the lightcurve. This would lead to a considerably more definitive linear phase function fit. However, we do not have sufficient coverage of the rotational phase to perform a meaningful Fourier analysis and cannot carry this analysis further at present.
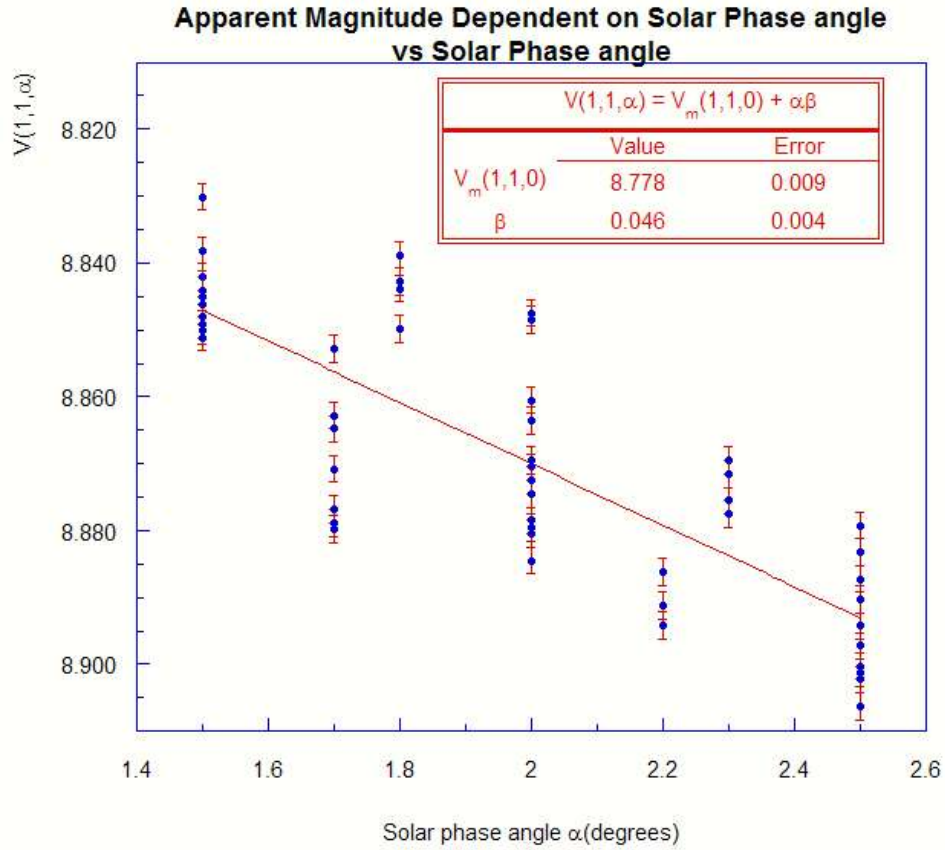
Figure 5.2: Apparent magnitudes, normalized to a heliocentric and geocentric distance of 1AU as a function of the solar phase angle. The vertical scatter is caused by the rotation of the object about its axis. The apparent magnitude increases with increase in solar phase angle (note the vertical axis is inverted). We cannot conclude that this is an opposition effect as we have do not have sufficient solar phase angle coverage to observe any non-linear decrease in brightness. Indeed the observed increase in brightness can be fit with a linear phase relation. We cannot therefore exclude the possibility that the observed trend of decrease in absolute magnitude evident in Fig. 5.1 is caused by the unsuitability of the IAU solar phase relation (Bowell et al; 1989) for 279 Thule, as was found to be the case for two similar objects 1173 Anchises and 2674 Pandarus (French, L.M., 1987). The discontinuity in magnitudes at phase angles of 1.7-1.8 and 2.2-2.3 is artifact of ephemeris that report phase angle to a tenth of a degree. The slope of the linear phase relation is more affected by the vertical scatter than this discontinuity and using more accurate values of phase angle will not change the fact that the magnitudes can be modeled by a linear phase relation.

All the remaining results in this section assume solar phase correction given by the standard IAU phase relation. We stress that the IAU phase relation is sufficient for several asteroids, but cannot describe the phase relation for all asteroids satisfactorily as shown by French (1987) and there is no compelling evidence that justifies using this solar correction for 279 Thule. We believe that caution must be used when applying solar phase angle corrections to C, D and P type asteroids, as they may have different surface properties from other outer-belt asteroids for which the phase relation was derived. We recommend further observations of these objects including 279 Thule near opposition over as wide a range of solar phase angle as is possible.

279 Thule was studied by Zappala et al. (1989) from 1984 Aug 21-23 in UBV using multiple telescopes at the European Southern Observatory (ESO) at solar phase angles with values (for each night) of 2.68, 2.93 and 3.18. The study did not correct for solar phase angle and reports mean apparent magnitudes dependent on solar phase angle (for each night) as 8.853, 8.856 and 8.878. These values match well with our apparent magnitudes '$V(1,1,\alpha)$' but at a lower range of phase angle. The discrepancy is small given the almost 19 years between the two sets of observations. The Planetary Data System (PDS) does give an absolute magnitude of 8.57 for 279 Thule based on this study and assuming the IAU solar phase relation. Again, this discrepancy is small given the time between the two sets of observations. Assuming this absolute magnitude, the IRAS Minor Planet Survey quotes an effective diameter of 126.59±3.7 and mean albedo of 0.0412±0.003.

The maximum observed difference in the absolute magnitude of 279 Thule is 0.07 and the maximum observed difference on any single night is 0.05. We prefer to report the size ratio using the second number as the phase angle varied much less on any given night than across the entire run. This difference in magnitude corresponds to a size ratio of 1.26:1. This represents a least size ratio and the actual variation of the lightcurve may be higher. Zappala et al. report an amplitude variation of the lightcurve of 0.06±0.01.

We attempted to extract a rotational period for 279 Thule using PDM. A high resolution PDM scan (see Fig. 5.4) determined the minimum value of the statistic 'Θ' to occur at a period of 7.6±0.5 hrs (hereafter, minimum period), which is comprable to the previously reported period of 7.44±0.01 hrs (Zappala et al; 1989). The error is computed using the width of the *pdm* scan near the minimum. A better estimate for the period requires more rotational phase coverage. Another period of 11.3 hrs was also found in the data (see Fig. 5.3). The *pdm* routine reports the first period as the true minimum in a high-resolution scan. The second period is almost exactly 1.5 times the minimum period. The structure around the minimum period is similar to the structure around the second period, and it appears that the structure around the second period is also scaled by this factor of 1.5. A period at 5.6 hrs is also found but is not as likely as the first two periods. It is almost exactly 0.75 times the minimum period. Interestingly, the structure around the minimum period also appears to be repeated around the 5.6 hrs period and scaled by a factor of 0.75. This aliasing is the result of insufficient coverage of the rotation phase. There is some uncertainty in the period because of aliasing, but we believe that the similarity between previous photometric measurements and period (Zappala et al; 1989)and ours

provides a strong case in favor of a period of 7.6±0.5 hrs determined by *pdm* to be the period that minimizes the scatter in a trial lightcurve.
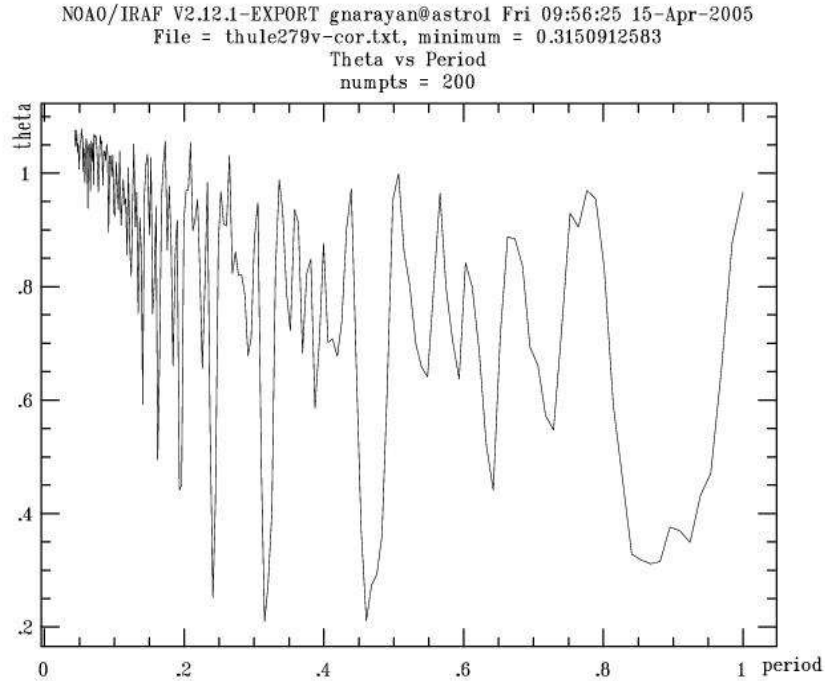

Figure 5.3: A PDM scan for asteroid 279 Thule reveals that the minimum value of the statistic 'Θ' (theta) occurs for a period of about 0.315-d or 7.6 hrs. The deep dip to the right of the minimum at approximately 0.470-d represents another candidate period of 11.3 hrs. We cannot totally reject this candidate period using PDM, as the value of 'Θ' for both periods is very comparable. The dip at approximately 0.235-d is simply half the 0.470-d period. Multiple periods such as these are a consequence of insufficient phase coverage for the object, and the problem that they present can only be resolved by simultaneous observations from another observatory in the world, or by observations of the same asteroid at a different epoch. A higher resolution scan to compare the two candidate periods is given below.
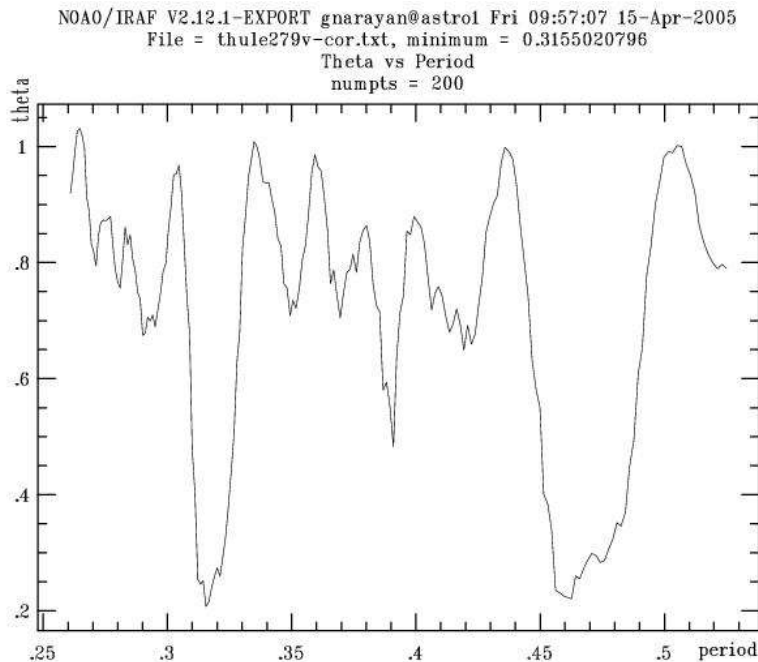
Figure 5.4: A PDM scan with a smaller baseline yields higher resolution. This scan allows for quantitative comparison of the two most likely periods – the two low dips in the graph symmetric about 0.316-d and 0.470-d respectively. This PDM scan also returned the 0.316-d period as the true period. The FWHM of the PDM scan near the minimum period is 0.02-d and we use this number to put a lower-bound on the error in the period. A better period can be determined with more rotational phase coverage.

35

5.5 Results for C/2002 CE$_{10}$ (LINEAR)

C/2002 CE$_{10}$ (LINEAR) was tracked siderealy from night 1 through 3. Its elongated appearance was thought to be the result of cometary activity that had been observed using the 8.2m Subaru telescope in August 2003 (Takato et al; 2003). However, when we tracked the telescope to compensate for the sky motion of the object, it became apparent that the elongation was entirely the result of the object's rapid sky motion. We therefore reject all data from nights 1 through 3. In addition, night 1 proved un-photometric. A failure of the telescope focus system on night 7 led to a halt in observing for more than an hour. CTIO personnel expertly repaired the problem and we resumed observing, but we found the object to be at an unacceptably high and increasing airmass. The few observations of the object made before the failure were not used in photometry as we had not made observations of standards at comparable airmass that early in the night.

The object was observed by Jewitt (2005) on 2003 Jan 8 at the 10m Keck telescope, and was found to have a mean absolute red magnitude of 13.12±0.02, and a mean V-R color index of 0.56±0.03. This gives an absolute visual magnitude of 13.68±0.05. This value is higher than our mean absolute visual magnitude of 13.11±0.01. This indicates that the object was fainter in January. However our mean V-R color index of 0.54±0.02, agrees with the given value. Jewitt also observed the object on 2003 Aug 28 at University of Hawaii (UH) 2.2-m telescope. He reports a mean absolute red magnitude of 12.53±0.02 for this date and a mean V-R color index of 0.53±0.02, and therefore a mean absolute visual magnitude of 13.06±0.04. This is in much closer to our result, indicating that the object's brightness in August is very close to its brightness in October. The Subaru observations of a faint tail in August 2003 provide the explanation for the 0.62 decrease in magnitude from January to August 2003. The corresponding increase in brightness is easily explained if the comet showed a coma. However, it is unlikely that a coma would cause a uniform increase in all absolute magnitudes, which is needed to explain the lack of variation in the V-R color from January to October, and other indices from January to August.

Jewitt argues that if the coma were sufficiently faint, it would not alter the color indices, as these are dependent only on the properties of the nucleus. We feel that this claim is difficult to justify, as our observations cannot distinguish between coma and nucleus, as Jewitt claims is possible with the UH 2.2-m observations. Yet UH 2.2m observations on 2003 Aug 28 agree very well with our observations from 2003 Oct 16-18. This implies that both sets of observations are almost certainly contaminated by near nucleus coma. This makes all photometry from this period suspect as aperture photometry yields the combined level of the nucleus and the coma, and an estimation of the background sky-level may not include the level from the coma, which might in addition be highly variable. We therefore cannot determine meaningful size ratios. We could not determine a rotational period for C/2002 CE$_{10}$ (LINEAR) using the PDM algorithm, as we were not able to get sufficient phase coverage for this object. Any rotational period would have also been based on the assumption that the coma remained constant, which is not justifiable.

6. ACKNOWLEDGEMENTS

REFERENCES

Abell, P. A., Fernández, Y. R., Pravec, P., French, L.M, Farnham, T. L., Gaffey, M. J., Hardersen, P. S., Kušnirák, P., Šarounová, L., Sheppard, S. S. and Narayan, G. S. 2005, "Characteristics of C/2001 OG$_{108}$" Icarus, (accepted)

Asher, D. J, Bailey, M. E., Hahn, G. and Steel, D. J. 1994, "Asteroid 5335 Damocles and its Implications for Cometary Dynamics", MNRAS **267**, 26

Bowell, E., Hapke, B., Domingue, D., Lumme, K., Peltoniemi, J. and Harris, A.W., 1989, "Application of Photometric Models to Asteroids", In **Asteroids *II***, eds. R. P. Binzel, T. Gehrels, and M.S. Matthews

Fernández, Y. R., Lisse, C. M., Ulrich, K. H., Peschke, S. B., Weaver, H. A., A'Hearn, M. F., Lamy, P. P., Livengood, T. A. and Kostiuk, T. "Physical Properties of the Nucleus of Comet 2 P/Encke" Icarus **147**, 145

Fitzsimmons, A., Williams, I.P., Lagerkvist, C.-I. and Dahlgreen, M., 1990, "Spectra of Six Asteroids Obtained at La Palma" MNRAS **247**, 26

French, L.M., 1987, "Rotation Properties of Four L5 Trojan Asteroids from CCD Photometry", Icarus **72,** 325

Hall, D.S. and Genet, R.M., 1982, Photoelectric Photometry of Variable Stars, IAPPP, Minuteman Press

Jewitt, D. 2005, "A First look at the Damocloids", AJ **129**, 204

Lagerkvist, C. –I., Williams, I.P. Fitzsimmons, A. and Dahlgreen, M. 1990, "(279) Thule", IAU Circular **4992**

Landolt, A.U. 1992, "UBVRI Photometric Standard Stars in the Magnitude Range 11.5-16.0 around the celestial equator", AJ **104**, 340

Levinson, H. F. and Duncan, M. J. 1997, Icarus **127**, 13

Lumme, K. and Bowell, E. 1981, "Radiative Transfer in the Surfaces of Atmosphereless Bodies. I. Theory", AJ, **88**, 1694

Massey, P. 1989, "The Stellar Content of Two OB Associations in the LMC: LH117 (NGC 2122) and LH118", AJ **97**, 107

Massey P. 1997, A User's Guide to CCD Reductions with IRAF

Marsden, B. G. 1986, "Notes from the IAU General Assembly Meeting", MPC No. **10193** and **10194**

McNaught, R. H., Stevens, B., Helin, E. F., Pravdo, S., Lawrence, K., Hicks, M., Hovland, E., Bickler, T., Schroeder, J., Scherr, L., Thicksten, R., Deetz, A., McGaha, J. E., Blythe, M., Shelly, F., Bezpalko, M., Huber, R., Manguso, L., Adams, S., Piscitelli, J., Stuart, J., Sayer, R., Evans, J. B., Viggh, H., Shelus, P. J., Laurie, S. P. and Marsden, B. G. 2002, "2002 CE10", MPEC No. **2002-C83**

Meech, K. J. and Belton, M. J. S, 1989, "(2060) Chiron" IAU Circular **4770**

Romanishin, W. 2002, "An Introduction to Astronomical Photometry Using CCDs", University of Oklahoma

Stellingwerf, R.F. 1978, "Period Determination using Phase Dispersion Minimization", ApJ **224**, 953-960

Takato, N., Sekiguchi, T. and Watanabe, J. 2003, "Comet C/2002 CE$_{10}$ (LINEAR)", IAU Circular **8193**

Vilas, F. and Smith, B. A. 1985, "Reflectance spectrophotometry (about 0.5-1.0 micron) of outer-belt asteroids - Implications for primitive, organic solar system material", Icarus **64**, 503

Walker, A., 2000, "CTIO CFCCD User Manual"

Young, A.T., 1974, Methods in Experimental Physics, **Vol. 12, A**, Academic Press, NY

Zappala, V., Di Martino, M., Cellino, A., Farinella, P., De Sanctis, G. and Ferreri, W. 1989, "Rotational Properties of Outer Belt Asteroids" Icarus **82**, 354

APPENDIX A

A.1 The Magnitude System

The idea of a magnitude system originated with the Greek astronomer, Hipparchus, who first classified stars by how bright they appeared to the naked eye. The brightest stars that Hipparchus could observe were assigned a magnitude of '1', the next brightest '2', and so on; to the faintest stars he could see, he assigned a magnitude of '6'. The system, while simple, understandably did not take into account the nature of the eye, which is not a good linear detector i.e. an object that emits twice as much light as another, does not appear twice as bright to the eye when we compare both objects with the naked eye. In addition, Hipparchus is the source of the inverted scale for magnitudes, as brighter objects have lower magnitudes.

Astronomers have adjusted the magnitude scale to make it more convenient, and a difference in magnitude of '1' corresponds to a constant brightness ratio. Specifically, Norman R. Pogson at Oxford University suggested that a difference of five magnitudes correspond to the object of lower magnitude being brighter than the object with a higher magnitude by a factor of 100; a suggestion that was quickly adopted. Finally, the zero point of the system was set by arbitrarily defining the magnitude of the star Vega to be exactly '0'. Better measurements of the magnitude of Vega, have determined that it actually has a magnitude of 0.03, but the scale had been too long in existence for it to be adjusted for this shift in origin. Thus, we can write the magnitude equation, in a variety of equivalent forms relating the magnitudes m_A, and m_B to the intensities I_A, and I_B.

$$\frac{I_B}{I_A} = 100^{\frac{(m_A - m_B)}{5}} \tag{A.1.1}$$

$$m_a - m_b = -2.5 \log\left(\frac{I_A}{I_B}\right) \tag{A.1.2}$$

How bright an object appears to us depends, in part, on our distance from it, specifically brightness varies as the inverse square of the distance to the object. This makes it difficult to compare the brightness of objects, and so the absolute magnitude 'M' is often used. The absolute magnitude is defined as the apparent magnitude 'm' of an object at a distance of 'd_A' parsecs, when normalized to a distance of 10 parsecs from us. This provides us with a way to compare the brightness of two objects directly, rather than just their apparent magnitudes. According to the inverse-square law,

$$\frac{I_A}{I_{10}} = \left(\frac{10 \, pc}{d_A}\right)^2 \tag{A.1.3}$$

$$M = m - 5 \log\left(\frac{d_A}{10 \, pc}\right) \tag{A.1.4}$$

This absolute magnitude is just one example of a normalized magnitude system; we can normalize magnitudes to any distance we choose. Absolute magnitudes for asteroids are

normalized to geocentric and heliocentric distances of 1AU and 0° solar phase angle. Absolute magnitudes for asteroids are not the same as absolute magnitudes normalized to 10 parsecs, despite both being referred to by the same name. Normalization is simply a method to remove the dependence of magnitudes on distances and provides a method to compare the brightness of two objects under similar conditions. By convention, instrumental magnitudes are reported with lower-case alphabets and absolute magnitudes, as well as those calibrated to some standard are referred to using upper-case alphabets.

The brightness of an object depends on what wavelength or color of light we are looking at, as objects have different spectra, and appear brighter in some colors than in others. Therefore, the magnitude of a star also depends on its color. Astronomers therefore split light from an object into various ranges of wavelengths using filters. The Johnson-Kron-Cousins BVRI system is just one such system of filters, and is used for most photometry. We can then use the absolute magnitude of a star, which usually refers to its visual or 'V' magnitude, and its colors '$B-V$', '$V-R$' and '$V-I$' or the difference between the magnitudes in any two filters.

A.2 The Point Spread Function

For photometric purposes, we can approximate all objects that we observe to be point sources of light as their actual sizes are small compared to their distance from us. However, we can never resolve a true point source, as several factors such as the atmosphere, telescope optics, and the fundamental fact that matter is not continuous, cause a blurring of the image. The largest source of blurring for ground-based observatories is the atmosphere. Any function that takes a point source of light, and returns a blurred image of it, is called a point spread function or PSF.

Mathematically, given some intensity distribution $I_o(y,z)$ in the object plane, an area element $dydz$ will emit a flux $I_o(y,z)dydz$. The PSF $\Gamma(y,z;Y,Z)$ causes a flux density of dI_i in the image plane, such that

$$dI_i(Y,Z) = I_o(y,z)\Gamma(y,z;Y,Z)dydz \qquad \text{(A.2.1)}$$

$$I_i(Y,Z) = \int_{-\infty}^{\infty}\int I_o(y,z)\,\Gamma(y,z;Y,Z)\,dy\,dz \qquad \text{(A.2.2)}$$

As the input is a point, the intensity distribution in the object plane can be modeled as the product of intensity of the point source 'A' and two Dirac delta functions, which make the intensity zero everywhere except at the point (y_o,z_o).

$$I_o(y,z) = A\delta(y-y_o)\delta(z-z_o) \qquad \text{(A.2.3)}$$

and, because of the integral properties of the delta function, this implies

$$I_i(Y,Z) = A\Gamma(y,z;Y,Z) \qquad \text{(A.2.4)}$$

Assuming a circular aperture, for a well corrected system, it can be shown that the PSF is nothing but the Airy distribution function, centered on the Gaussian image point (see Fig. A.2.1). A full derivation of this result is available in any textbook on Fourier optics. In spherical coordinates the intensity in the image distribution in the image plane $I_i(r)$

$$I_i(r) = \frac{I_i(0)}{\pi} \left(\frac{J_1(v_c r/2)}{r} \right)^2 \tag{A.2.5}$$

where 'J_1' is the first order Bessel function (of the first kind) (see Fig. A.2.2).

$$J_1(u) = \frac{-i}{2\pi} \int_0^{2\pi} e^{i(v + u\cos(v))} \, dv \tag{A.2.6}$$
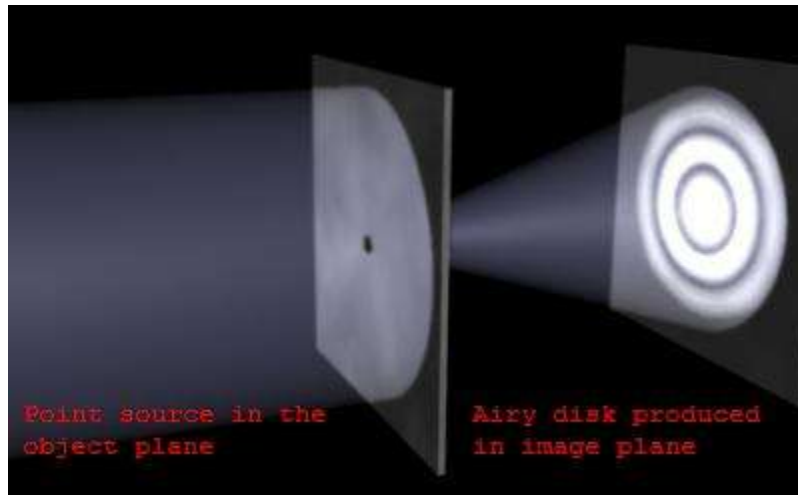

Figure A.2.1: When a point source of light undergoes Fourier diffraction through a circular aperture, the resulting intensity distribution in the image plane is called the Airy disk. (Source: Astrophysics, and Space Research Group, University of Birmingham)
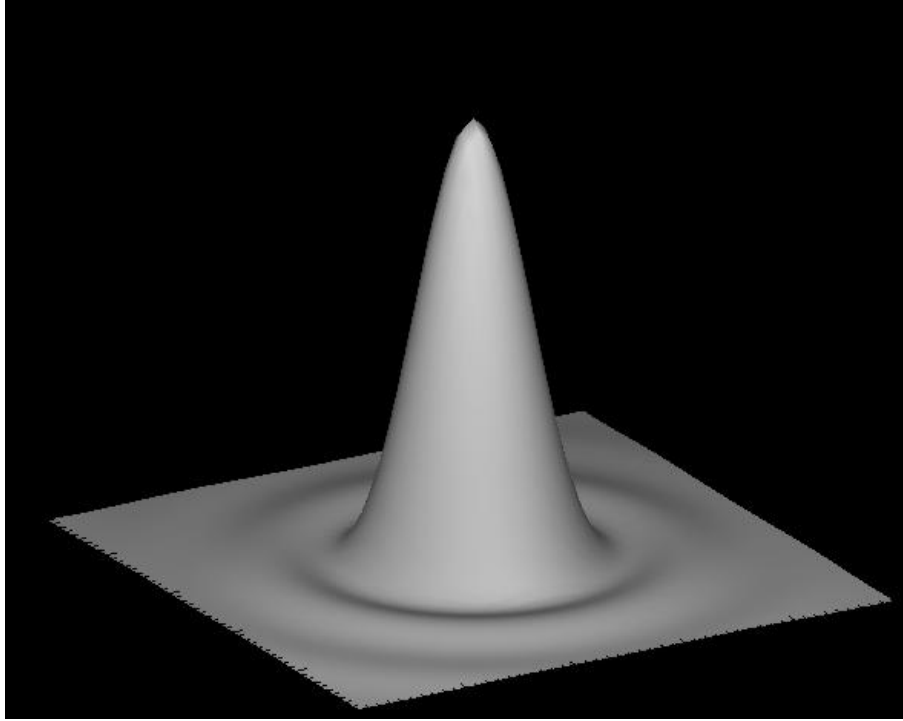
Figure A.2.2: The Airy distribution is expressed using equation. A.2.5. The first order Bessel function, is an oscillatory function that decays with increase in radius from the center. As the distribution is circularly symmetric, we can make radial profiles of it such as in Fig. 2.5. (Source: Alexei Tokovnin, CTIO)

As the Bessel function approaches zero asymptotically, we can never determine the full intensity distribution of an object. We therefore use fixed aperture photometry, as described in Chapter 4, to estimate the intensity of the object, and therefore get apparent or instrumental magnitudes, using the magnitude equation.

A.3 Atmospheric Extinction and the Transformation Equations

As light passes through the atmosphere, photons can either be scattered in random directions or absorbed, either partially or completely by molecules. The net result is a dimming or partial extinction of the starlight, which can be described in terms of a transparency of the atmosphere. The transparency depends on the wavelength of light, and can be variable across the sky, and with time for example, fine structured and rapidly moving cirrus clouds make photometry impossible (Hall and Genet, 1982). In order to do photometry, the transparency must not vary strongly with sky position, and must remain stable throughout the night.

This transparency can be modeled much the same way that opacity is modeled. We can idealize the earth's atmosphere as a plane parallel layer with uniform opacity along the horizontal and the vertical. The height of the slab, as measured from the observatory to the top of the slab is defined as one airmass. The "zenith distance" of a star is the angle between the observer's zenith and the line connecting the observer and the star. The

length of the slab at any given zenith distance 'z' is called the airmass 'X' and in this model (see Fig. A.3.1) can be expressed using the simple relation

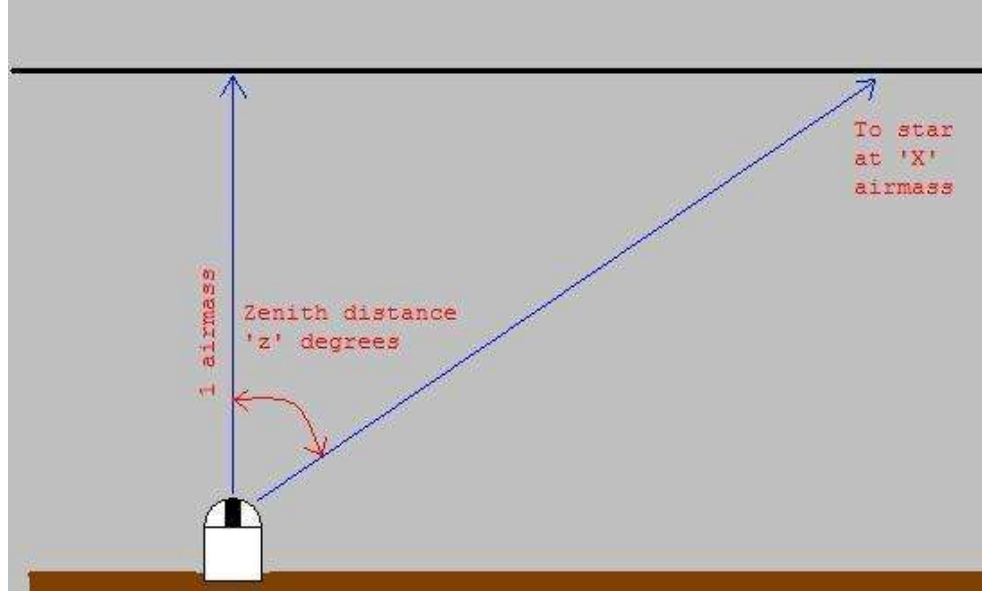$$X = sec(z) \tag{A.3.1}$$

Figure A.3.1: The slab model of the atmosphere can be used to approximate the airmass, using relation A.3.1. The atmospheric extinction is accounted for when solving the transformation equations (equation 4.2) to convert from instrumental to magnitudes in the Johnson-Kron-Cousins system.

There are obvious limitations to the slab model of the atmosphere such as the atmosphere not being a slab. Rather, it curves with the surface of the earth, does not have a well defined edge, its density and therefore its opacity depends on height, and wavelength of light. By restricting photometry to small values of the airmass, we can minimize the problem somewhat. Thus, in this work, we do not use 'X' >1.6 to do photometry. Young (1974) give a more accurate formula

$$X = sec(z)[1-0.0012(sec(z)-1)] \tag{A.3.2}$$

that is found to work well up to $sec(z) = 4$ (Hall and Genet, 1982). If very high accuracy airmass' are needed, even down to the horizon, where observations are limited by light blocks such as other observatories on site, Romanishin (2002) gives

$$X=sec(Z)-0.00186(sec(z)-1)-0.002875(sec(z)-1)^2-0.000808(sec(z)-1)^3$$
$$\dots \text{(A.3.3)}$$

The intensity modeled as decaying exponentially with airmass 'X' such that

$$I = I_o e^{-E_\lambda X} \tag{A.3.4}$$

where 'I_o' is the intensity that would be observed without the effect of the atmosphere, 'I' the intensity after atmospheric extinction, and 'E_λ' is some constant of proportionality. Therefore, using the magnitude equation discussed in appendix A.1, the observed or instrumental magnitude 'm' is related to the magnitude that we would observe without atmospheric extinction (i.e. at zero airmass, ZAM) 'm_o' by

$$m = m_o - E_\lambda X \qquad (A.3.4)$$

The ZAM color terms (i.e. without atmospheric extinction) are not exactly the same as the color terms of the standard system. The ZAM color terms depend on the instrumental magnitudes which in turn are dependent on the filter system, detector, observing site etc. However, the filter-detector system is chosen to match the standard system as closely as possible and therefore the differences between the two systems should be small and systematic. Therefore, the color terms can be modeled as a simple linear transformation from the standard color terms, for example,

$$v_o - r_o = K_m + C_m (V-R) \qquad (A.3.5)$$

Combining equations A.3.4 and A.3.5 allows us to account for atmospheric extinction and detector characteristics, and these transformation equations allow us to convert between instrumental magnitudes and magnitudes in the Johnson-Kron-Cousins system. The coefficients of the transformation equations are determined by fitting the measured instrumental magnitudes of the standard stars to the magnitudes of the stars as measured by Landolt (1992).

APPENDIX B

B.1 Charge Coupled Devices

Invented in 1970 by Willard Boyle and George Smith at Bell Laboratories, the charge-coupled device (CCD) has become the standard photo-electronic imaging device in astronomy. CCDs are constructed out of a chip of crystal silicon that is logically divided into a two dimensional array of picture elements or "pixels." The CCD consists of polysilicon electrodes or "gates" with metal contacts, separated from a p-type semiconductor by a thin layer of oxide, usually silicon dioxide. This structure is common in electronics and is called a metal oxide on semiconductor (MOS) capacitor. Three of these MOS capacitors constitute one pixel.

The use of a p-type semiconductor causes the hole concentration at equilibrium to be much larger than the electron concentration. When a positive voltage is applied to the gates, it repels the holes and creates a depletion region near the semiconductor-oxide interface. When the semiconductor is exposed to light, electrons are ejected via the photoelectric effect, and are attracted towards the gates and accumulate in the depletion region. Effectively, the electrons are trapped in a potential well. The photocurrent is directly proportional to the intensity of the incident light, over a large range of intensities, and therefore the CCD is a linear photosensitive detector. Electronics can control exactly how long the gate voltage is applied, and therefore control how long the MOS capacitors store charge, or how long the CCD integrates. Thus, CCDs can be shuttered electronically as well as physically.

When two gates are sufficiently close to each other, their potential wells merge. If the voltage of one gate is higher, than the neighboring gate, then electrons will be transferred to the potential well of the gate with a higher potential. A clocking mechanism regulates the potential difference between the three gates, and facilitates the transfer of charge from one gate to another. The third gate separates each pair of gates while the charge is transferred between them. In order to control a gate chain of any length, only three separate clocking signals are needed. The clocking signals are square waves with a 120º phase shift between them. Readout of the CCD involves clocking each row of pixels simultaneously, and shifting the stored charge, one by one towards a serial register that is connected to an output amplifier and a digitizer. The output is therefore a pixel-by-pixel representation of the image produced in the CCD. The charge transfer efficiency (CTE) is the percentage of charge transferred from one pixel to another. Most research grade CCDs have better than 99.999% CTE.

The quantum efficiency (QE) of a CCD is a measure of the efficiency with which incident photons are detected. Some incident photons may be reflected, or absorbed in a region of the semiconductor from which electrons cannot be absorbed. The QE depends on the wavelength of the incident light. In front-illuminated CCDs, incident photons pass through the gate structure before they can generate electrons. Silicon has a high absorption coefficient for short wavelength photons, and therefore front-illuminated CCDs have low QE in the blue and UV. In back-illuminated CCDs, the incident light

falls directly on the silicon crystal that is thinned to around 15-20 microns. This process enhances the QE in the blue and UV. The QE of back-illuminated CCDs is often further enhanced by using anti-reflective coatings.

B.2 Quantum Efficiency of our CCD, and Filter Transmission Curves
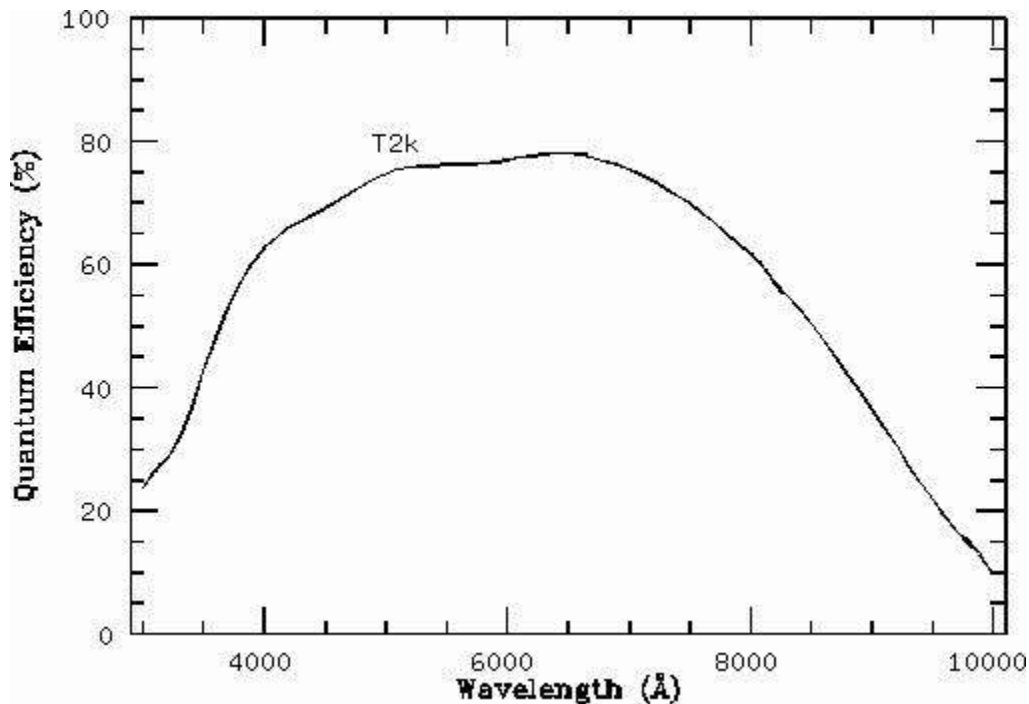

Figure B.1: The QE curve of the TeK 2K CCD, such as that mounted on the 0.9m SMARTS telescope at CTIO. The CCD has better than 50% QE from 400-850nm. (Source: Alistair Walker, CTIO)

The percentage of the incident light detected does not depend solely on the QE of the CCD, as the light passes through filters before it is incident on the CCD. The fraction of the incident signal that is detected is the convolution of the filters transmission curve, and the QE curve of the CCD.
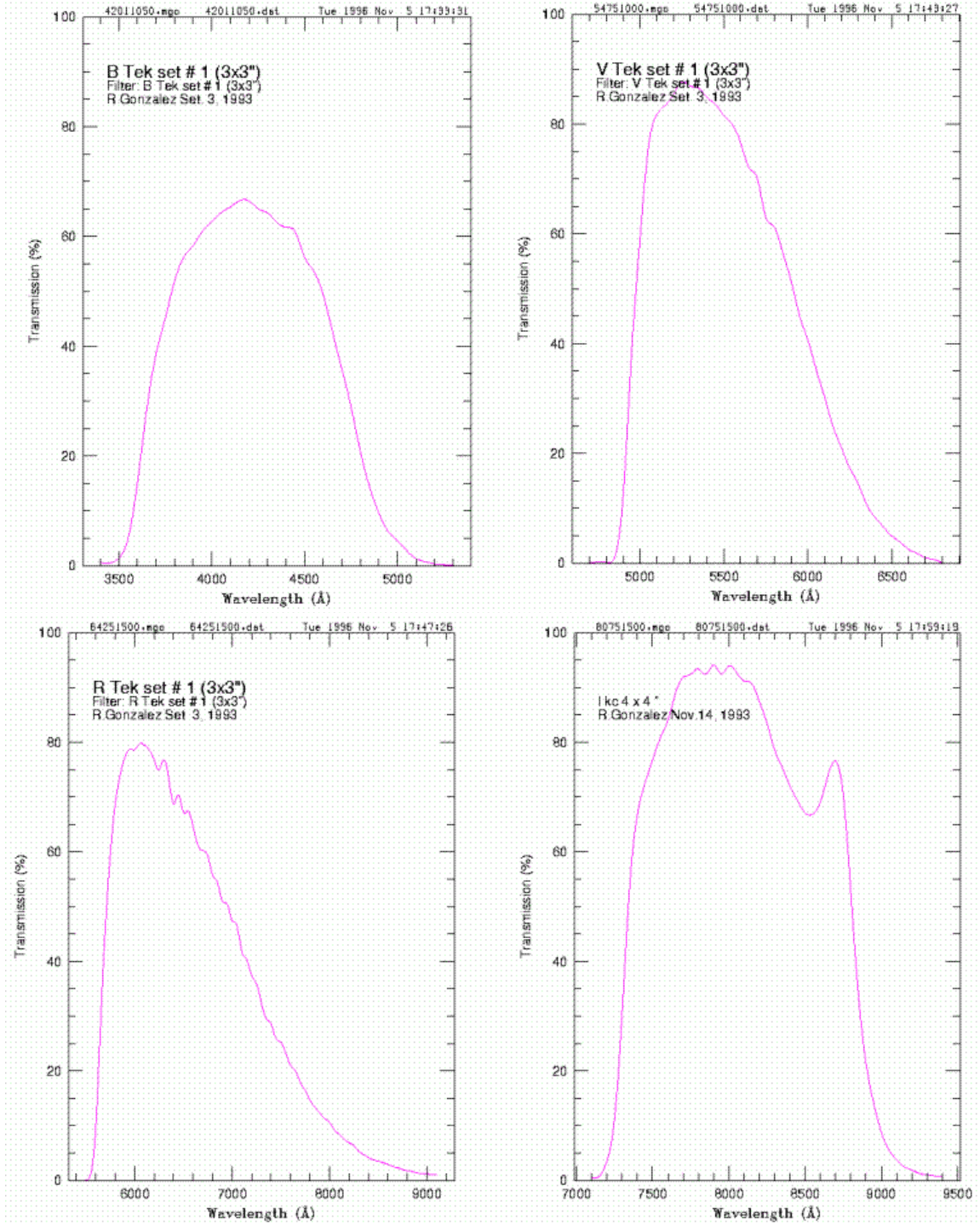
Figure B.2: Transmission curves for the set of filters used in this observing run (clockwise from top left) approximate the Johnson 'B' and 'V', Cousins 'R' and Kron 'I' filters. CTIO personnel periodically check the filters to ensure that their transmission characteristics have not changed significantly. The transformation equations allow us to remove the effects of our particular filter system. The Kron 'I' filter is wrongly listed as 4x4" as a check of the serial number on the top left of the graph reveals. (Source: Ricardo González, CTIO)